X-ray transient absorption structural characterization of the 3MLCT triplet excited state of cis-[Ru(bpy)2(py)2]2+

X-Ray Transient Absorption Structural Characterization of the ^{3}MLCT Triplet Excited State of *cis*-$[Ru(bpy)_2(py)_2]^{2+}$

Elisa Borfecchia, Claudio Garino, Luca Salassa, Tiziana Ruiu, Diego Gianolio, Xiaoyi Zhang, Klaus Attenkofer, Lin X. Chen, Roberto Gobetto, Peter. J. Sadler, and Carlo Lamberti

Dalton Trans., **2013**, *42*, 6564–6571

doi: 10.1039/c3dt32865a

X-Ray Transient Absorption Structural Characterization of the ^{3}MLCT Triplet Excited State of *cis*-$[Ru(bpy)_2(py)_2]^{2+}$

Elisa Borfecchia,[1] Claudio Garino,[1] Luca Salassa,[2#]* Tiziana Ruiu,[1] Diego Gianolio,[1] Xiaoyi Zhang,[3] Klaus Attenkofer,[3] Lin X. Chen,[3,4] Roberto Gobetto,[1] Peter. J. Sadler,[2] and Carlo Lamberti[1]*

[1] Department of Chemistry and NIS Centre of Excellence
University of Turin
via P. Giuria 7, 10125 Turin (Italy)
Fax: (+39) 011 6707882
E-mail: carlo.lamberti@unito.it

[2] Department of Chemistry
University of Warwick
Gibbet Hill Rd, Coventry CV4 7AL (UK)

[3] X-ray Science Division and Chemical Sciences & Engineering Division
Argonne National Laboratory
9700 South Cass Ave., Argonne, IL 60439 (USA)

[4] Department of Chemistry
Northwestern University
2145 Sheridan Road, Evanston, IL 60208 (USA)

[#] Current address: CIC biomaGUNE
Paseo Miramón 182, 20009 Donostia–San Sebastian (Spain)
Fax: (+34) 943 005301
E-mail: lsalassa@cicbiomagune.es

ABSTRACT

The excited state dynamics and structure of the photochemically active complex *cis*-$[Ru(bpy)_2(py)_2]^{2+}$ have been investigated using optical transient absorption (OTA) and X-ray transient absorption (XTA) spectroscopy and density functional theory (DFT). Upon light-excitation in aqueous solution *cis*-$[Ru(bpy)_2(py)_2]^{2+}$ undergoes ultrafast dissociation of one pyridine ligand to form *cis*-$[Ru(bpy)_2(py)(H_2O)]^{2+}$. OTA measurements highlighted the presence of two major time components of 1700 ps and 130 ps through which the system decays to the ground-state and evolves towards the photoproduct. XTA data were acquired after 150 ps, 500 ps, and 3000 ps from laser excitation (λ_{exc} = 351 nm) and provided the transient structure of the ^{3}MLCT state corresponding to the longer time component in the OTA experiment. In excellent agreement with DFT, XTA shows that the ^{3}MLCT geometry is characterized by an elongation of the dissociating Ru−N(py) bond and a shortening of the *trans* Ru–N(bpy) bond with respect to the ground state. Conversely, calculations show that the ^{3}MC state which has a highly distorted structure with Ru–N(py) bonds between 2.77 – 3.05 Å.

INTRODUCTION

Over the past ten years, time-resolved X-ray techniques[1-3] have emerged as new formidable tools to investigate electronic and molecular structures of light-generated short-lived species. Ultrafast laser pulse excitation coupled with time-resolved X-ray absorption spectroscopy (XAS), X-ray diffraction and X-ray scattering have led to cutting-edge advances in our knowledge of the photochemistry and photophysics of a wide range of systems, from small fundamental molecules[4, 5] to large proteins.[6, 7]

In particular, X-ray transient absorption (XTA) spectroscopy has been implemented for the study of the excited-state structures of metal coordination compounds. This method captures transient structural information by measuring differences in XAS spectra of optically-excited (i.e. excited state, ES) and unexcited (i.e. ground state, GS) molecules. Compared to other time-resolved X-ray techniques, XTA has the advantages of probing transient local electronic structures and nuclear geometry with high selectivity and precision, which is very important for understanding the influence of structural factors in chemical reactions.[1, 2, 8]

XTA has provided unprecedented insights into the mechanism of axial photoligation and photodissociation of coordinating solvent molecules in nickel porphyrins, such as $[Ni(TPP)L_2]$ and [Ni(TMP)] (where TPP = tetraphenylporphyrin, TMP = tetramesitylporphyrin and L = piperidine).[9-11] The method has also elucidated light-induced structural changes resulting from the excited state of $[Ru(bpy)_3]^{2+}$,[12] and from the ultrafast spin crossover in $[Fe(bpy)_3]^{2+}$.[13] Moreover, in the case of $[Cu(dmp)]^{2+}$ (where dmp = 2,9-dimethyl-1,10-phenanthroline) in acetonitrile, XTA tracked the formation of a MLCT (metal-to-ligand charge transfer) state – solvent adduct responsible for quenching the complex's luminescence.[14] Recently, XTA was employed to elucidate the structural distortions of the photochemically active di-platinum complex $[Pt_2(P_2O_5H_2)_4]^{4-}$,[15] and a pyrazolate bridged platinum dimer.[16, 17]

These studies are fundamental steps towards a full understanding of excited-states and nuclear and electronic structures of metal complexes which are ultimately connected to applications in solar energy conversion,[18] catalysis,[19] bioinorganic[20] and medicinal chemistry.[21] Indeed, XTA and time-resolved X-ray-based techniques in general complement other spectroscopic findings by disclosing precise information on transient structures at the atomic level. In addition, such a method is attractive in providing unique experimental benchmarks for computational photochemistry, a growing field with outstanding potential for studying excited-state reaction mechanisms and for guiding the design of innovative photoactive chemicals.

In the last few years, we and others have developed promising light-activated ruthenium polypyridyl complexes as novel anticancer agents[22-24] and as cage compounds for the release of bioactive ligands.[25, 26] The photorelease of a pyridine ligand is the key event in the mechanism of action of these systems and a thorough understanding of such process is vital for improving their design for biological applications.

Experimental studies on polypyridyl complexes have highlighted that photosubstitution is triggered by a photoactive ^{3}MC (metal-centered, d–d ligand field) state under a kinetic equilibrium with the ^{3}MLCT state generated via intersystem-crossing from the Franck-Condon ^{1}MLCT state. It is commonly believed that short-lived ^{3}MC states display significantly distorted geometries and are associated with

the quenching of optically-active ^{3}MLCT states via nonradiative decay to the ground state.[27-31] This latter aspect is also fundamental in many of the aforementioned applications where the lifetime of the redox active ^{3}MLCT state is crucial. Temperature dependence of the ^{3}MLCT luminescence lifetime has been used to investigate the interconversion kinetics of the ^{3}MLCT and ^{3}MC states in several $[Ru(bpy)_2L_2]^{n+}$complexes.[27, 30] However, since the ^{3}MC state is non-emissive, it is still unclear whether the ^{3}MC is the lowest-energy state from the relaxation of the ^{3}MLCT state.

A prototypic complex to study pyridine photorelease is *cis*-$[Ru(bpy)_2(py)_2]^{2+}$. In this system, ligand dissociation upon UV and visible excitation occurs with high yield (ca. 20%),[32] and is followed by coordination of a solvent molecule to give a photoproduct such as *cis*-$[Ru(bpy)_2(py)(H_2O)]^{2+}$ (PHP). For *cis*-$[Ru(bpy)_2(py)_2]^{2+}$ in solution, irreversible population of the ^{3}MC state from the ^{3}MLCT is believed to occur (Figure 1).[27-29, 33] Consistently, previous computational studies highlight that the ^{3}MC is likely to be the lowest-lying triplet excited state in *cis*-$[Ru(bpy)_2(py)_2]^{2+}$ and its population occurs through a ^{3}MLCT – ^{3}MC potential energy surface crossing. DFT shows that ^{3}MC states have dissociative character due to the population of σ-antibonding orbitals with a high metal d-orbital component.[34, 35]

Earlier, we reported a computational investigation of the singlet and triplet excited state manifold of *cis*-$[Ru(bpy)_2(py)_2]^{2+}$[34] and showed how TR-WAXS (Wide Angle X-ray Scattering) can fully capture in the scattering images (although in a quasi-static mode) structural changes triggered by light excitation.[36] Here the integration of XTA, optical transient absorption (OTA) measurements and DFT (density functional theory) calculations provide unprecedented insights into the sub-nanosecond photochemical timescale of the pyridine release and the ^{3}MLCT excited-state structure of *cis*-$[Ru(bpy)_2(py)_2]^{2+}$.

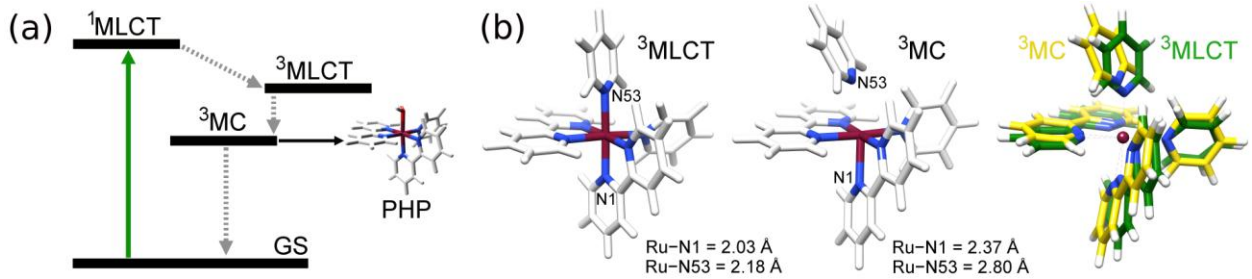

Figure 1. (a) Schematic excited state diagram for *cis*-$[Ru(bpy)_2(py)_2]^{2+}$; PHP = *cis*-$[Ru(bpy)_2(py)(H_2O)]^{2+}$. (b) DFT-optimized ^{3}MLCT and ^{3}MC structures in water (PBE0/LanL2DZ/6-311G**) and their superimposition.

RESULTS AND DISCUSSION

Geometry optimizations of the lowest-lying triplet state geometry of *cis*-$[Ru(bpy)_2(py)_2]^{2+}$ in water were performed with various functionals and basis sets and including solvent effects. Two minima corresponding to the ^{3}MLCT and ^{3}MC states were obtained regardless of the method used (Supporting Information Section A). Remarkably, in all cases the latter state is more stable by 0.28 – 0.91 eV. The geometries optimized at the PBE0/LanL2DZ/6-311G** level are chosen for discussion and were employed as starting guesses for XTA data analysis (*vide infra*) on the basis of the PBE0 functional performance.

In the ^{3}MC state, the Ru–N1(bpy) and Ru–N53(py) distances are significantly elongated (to 2.37 and 2.80 Å respectively) compared to the ^{3}MLCT (2.03 and 2.18 Å) and GS (2.08 and 2.16 Å) geometry. The ^{3}MC also significantly deviates from an ideal octahedral geometry with the py relative to the Ru–N53 bond bending towards one of the bpy ligands (Figure 1b).

Conversely, the ^{3}MLCT is more similar to the GS although Ru–N(bpy) distances are on average shorter compared to the GS, and the Ru–N(py) distances slightly longer. It is worth noting that excited-state Ru–N distances are quite insensitive to the method of calculation, with variations smaller than 0.023 Å, except in the case of the ^{3}MC Ru–N53(py) which lengthens to between 2.77 and 3.05 Å. This variability is likely related to difficulties of the ECP in modelling the two unpaired d-electrons in the ^{3}MC state. Spin density surfaces and time-dependent DFT (TDDFT) triplet transitions calculated using the two lowest-lying geometries confirm the metal-centered and charge-transfer nature of these states (Tables SIA1 – A3).

Optical Transient absorption (OTA) spectra (300 fs – 3 ns) of *cis*-$[Ru(bpy)_2(py)_2]Cl_2$ in aqueous solution (λ_{exc} = 390 nm, fwhm ~150 fs) are shown in Figure 2 (20 – 2860 ps) and in Section B of the Supporting Information (Figure SIB1 – B2, Table SIB1). Decay fittings over the whole range of wavelengths give two major time components, ~ 130 ps and ~ 1700 ps. For delays < 20 ps a third shorter time component of ~ 1.3 ps is observed. This is visible as a small decrease in intensity over time in the 500 – 550 nm range (Figure SIB1 – B2). As discussed by others,[37] such component can be attributed to a series of ultrafast processes, including intersystem crossing, internal conversion and vibrational cooling. In Figure 2, the negative band at 450 – 500 nm is predominantly due to the ground state bleach, while the broad positive signal at 525 – 750 nm can be ascribed to the ^{3}MLCT state absorption of $[Ru^{III}(bpy)(bpy^{-})(py)_2]^{2+}$, inducing transitions to upper excited states. Limited recovery of the ground state bleach (450 – 500 nm) within 20 ps delay is observed, consistent with the population decay of the ^{3}MLCT state (Figure SIB1).

The presence of two time components throughout the spectrum indicates that two intimately-connected processes are occurring. The 1700 ps time component can confidently be attributed to such a ^{3}MLCT state, in agreement with the low-temperature fluorescence lifetime value of 2.7 ns (acetonitrile) reported previously.[28] The shorter time component (130 ps) is more difficult to assign unequivocally. However it is not unreasonable to associate it to the ^{3}MC-mediated photochemistry pathway of *cis*-$[Ru(bpy)_2(py)_2]^{2+}$.[33, 38, 39] The presence of a static offset in the biexponential fitting parameters, particularly evident in the PHP absorption range, seems consistent with this scenario.

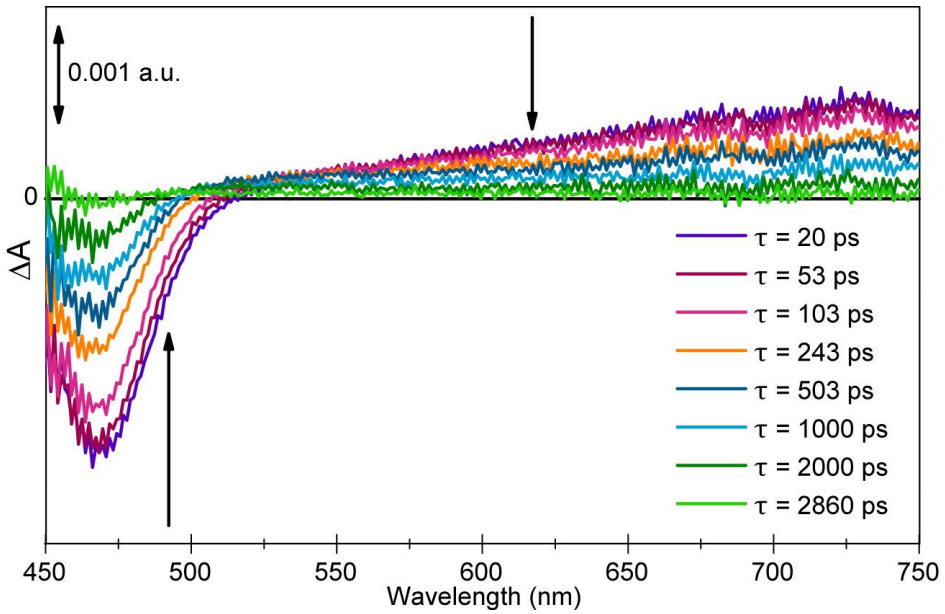

Figure 2. Transient absorption spectra of *cis*-$[Ru(bpy)_2(py)_2]Cl_2$ in aqueous solution (0.2 mM) collected in the 20 – 2860 ps time interval (λ_{exc} = 390 nm).

The described DFT and OTA information can be used to assist analysis of the XTA experiment we performed at the 11ID-D beamline of the APS (Advanced Photon Source, Argonne, USA) in order to achieve a thorough knowledge of the atomic rearrangements of *cis*-$[Ru(bpy)_2(py)_2]^{2+}$ in the excited states. The full experimental details and data reduction procedures are described in the Material and Methods and Supporting Information (SIC1, SIC2) sections. Ru K-edge XAS spectra were acquired after 150 ps, 500 ps, and 3000 ps from laser excitation (λ_{exc} = 351 nm), as well as for the unexcited complex (employed as reference for GS structure in the data analysis). We focused on the EXAFS region of the XAS spectrum for its strong dependency on bond distances, and for the lack of well-defined pre-edge features in the XANES of *cis*-$[Ru(bpy)_2(py)_2]^{2+}$, mostly due to the broadening induced by the K-hole lifetime.[40]

To interpret the transient EXAFS signal we applied a method recently proposed for the XTA structural analysis of the photoexcited $[Pt_2(P_2O_5H_2)_4]^{4-}$ ion.[15] According to this approach, the experimental differential EXAFS spectrum $\Delta\chi(q,\tau) = \chi^{ES}(q,\tau) - \chi^{GS}(q)$[41] at the time-delay τ is refined directly in momentum space by R-factor minimization between a large series of simulated differential curves and the experimental data (SIC3). Each simulated transient spectrum corresponds to systematic variations of fitting parameters obtained from the GS EXAFS analysis (e.g. Ru–N distances, Debye-Waller factors, edge energy shift). Moreover, a careful preparatory analysis of the GS complex and PHP structural features is necessary for this task and was therefore initially performed (SIC4, SIC5). Characterization of PHP structure is indeed crucial for the simulation of the time-resolved data since such species makes an important contribution to the total time-dependent differential signal. A comparison between first shell $R_{Ru-N(L)}$ bond distances (where L = bpy, py, H_2O) for GS and aqua photoproduct PHP obtained from EXAFS refinement and DFT geometry optimization is reported in Table 1.

Table 1. DFT (PBE0/LanL2DZ/6-311G** level) and EXAFS first shell $R_{Ru-N(L)}$ bond distances (where L = bpy, py, H_2O) for GS and PHP. Bond distances were obtained by standard EXAFS fit in the case of GS and by differential analysis in the case of PHP. DFT bond lengths were separately averaged for each type of ligand L.

Optimized Structural Parameters for GS and PHP				
Parameters	DFT optimization		EXAFS fit	
	GS average bond lengths	PHP average bond lengths	GS (Standard analysis)	PHP (Differential analysis)
$R_{Ru-N(bpy)}$ (Å)	2.08	2.07	2.05 ± 0.02	2.05 ± 0.01[a]
$R_{Ru-N(py)}$ (Å)	2.14	2.13	2.09 ± 0.05	2.07 ± 0.01
$R_{Ru-O(H2O)}$ (Å)	-	2.21	-	2.12 ± 0.01

[a] The error on PHP $R_{Ru-N(L)}$ bond distances corresponds to the step separating two contiguous nodes on the minimization grid employed.

In the GS, Ru−N(bpy) and Ru−N(py) distances are in good agreement with the calculated bond lengths, although slightly shorter as already found for this complex and other analogues.[42, 43] Standard EXAFS analysis of the PHP does not discriminate between the structural differences of the starting GS complex and *cis*-$[Ru(bpy)_2(py)(H_2O)]^{2+}$. Instead, using differential analysis, we identified a Ru−O distance of 2.12 Å, corresponding to pyridine substitution by a H_2O molecule.

After performing this key task, we estimated the populations of both ^{3}MLCT and the PHP for the three time-delays investigated by XTA. To this aim we started from the widely accepted general scheme for the excited-state dynamics of ruthenium polypyridyl complexes, reproduced in Scheme 1.

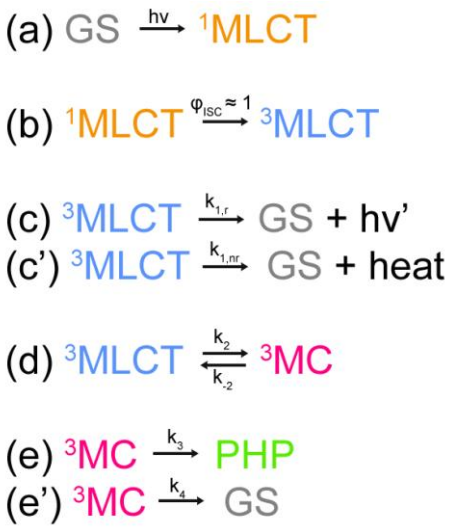

Scheme 1

In the specific case of aqueous *cis*-$[Ru(bpy)_2(py)_2]^{2+}$, $k_{1,r}$ and $k_{1,nr}$ (eq. c and c' in Scheme 1) can be considered as negligible. Moreover $k_{-2} << k_2$, resulting in irreversible population of the ^{3}MC state from the ^{3}MLCT.[27-30] According to such a scenario and considering the OTA time components together with a 20% photochemical yield φ, the populations of the ^{3}MLCT ES and PHP species, that mainly contribute to XTA signal at the investigated time-points, can be calculated (see Supporting Information SIC6.1) and are represented in Figure 3.

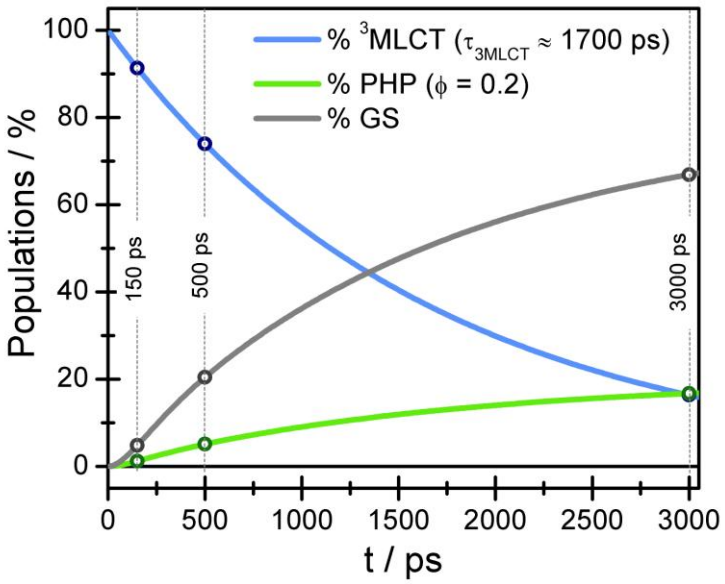

Figure 3. Time evolution of ^{3}MLCT population (blue solide line) and PHP percentage (green solid line) calculated according to Scheme 1. Circles and vertical dashed lines are placed in correspondence of the XTA experimental time delays.

Such information was employed to orientate the XTA differential fitting procedure. In particular, simulation of the XTA data was performed applying a fitting strategy based on the combined differential structural refinement of the PHP and the long-lived ^{3}MLCT components. The shorter OTA time component was not included in the fit model since this contribution is negligible at the investigated time delays with respect to the ^{3}MLCT. The fit amplitudes (f^{PHP} and f^{3MLCT}) of the PHP and ^{3}MLCT components were constrained according to their estimated ratio (see Supporting Information SIC6). More than one-hundred ^{3}MLCT structures were tested by systematically modifying the DFT-optimized geometry. Operatively, the two Ru–N1(bpy) and Ru–N53(py) bond lengths among all the others were conveniently selected as key structural parameters ($R_{Ru–N1}$, $R_{Ru–N53}$) to be optimized in the XTA fitting procedure. In fact, DFT geometry optimization calculations highlighted that Ru–N1(bpy) and Ru–N53(py) are the most affected distances by formation of the ^{3}MLCT state. The other Ru–N bonds vary less significantly with respect to the GS structure (C2 symmetry). Equivalent results are expected in the case the other py unit and the bpy ring *trans* to it are considered for the XTA fitting procedure, namely the Ru–N42(py) and Ru–N13(bpy) bonds (Supporting Information, SIA1-2). Each simulated curve $\Delta\chi_{fit}(q,\tau)$ is then described by Eq. 1:

$$\Delta\chi_{fit}(q,\tau) = f^{PHP}(\tau)\Delta\chi^{PHP}(q) + f^{^3MLCT}(\tau)\Delta\chi^{^3MLCT}(R_{Ru-N1}, R_{Ru-N53}, q) \qquad (1)$$

Adopting this approach in the analysis of the 500 ps and 3000 ps time delays disclosed the ^{3}MLCT excited-state structure. As a control, the same approach was employed using the ^{3}MC distorted geometry and optimizing the same Ru–N distances. In such case, corresponding to a long-lived ^{3}MC and to different excited-state populations, the fit quality is significantly worse. A full description of the

fitting procedure and a comparative summary of the results obtained using different excited-state population and geometry guesses is provided in the Supporting Information (SIC6).

Table 2. Best-fit values obtained for the ^{3}MLCT selected first shell Ru–N bond distances, $R_{Ru–N1}$ and $R_{Ru–N53}$, from XTA differential refinement, compared with corresponding DFT-optimized bond lengths.

^{3}MLCT ES structural parameters from XTA analysis and DFT geometry optimization					
τ (ps)	$R_{Ru–N1}$ (Å)		$R_{Ru–N53}$ (Å)		Best fit R-factor
	TR-EXAFS	DFT	TR-EXAFS	DFT	
500	2.03±0.02[a]	2.03	2.20±0.02	2.17	0.180
3000	2.03±0.02		2.16±0.02		0.378

[a] The error on bond distances from XTA analysis corresponds to the step separating two contiguous nodes on the minimization grid employed.

The $R_{Ru–N1}$ and $R_{Ru–N53}$ values reported in Table 2 highlight that the ^{3}MLCT geometry is characterized by a contraction of the Ru–N1(bpy) bond relative to the bpy unit in *trans* position to the py undergoing dissociation, and by an elongation of the Ru−N53(py) bond with respect to the GS. The $R_{Ru–N1}$ distance changes from 2.05 Å in the GS to 2.03 Å in the ^{3}MLCT for both delays, while $R_{Ru–N53}$ increases from 2.09 Å to 2.20 Å and 2.16 Å for 500 ps and 3000 ps, respectively. The small difference between the $R_{Ru–N53}$ values obtained at these two time-delays is likely to be due to differences in the population of the ^{3}MLCT state. Since the population of the ^{3}MLCT state is higher at 500 ps (74%) than at 3000 ps (16%), the bond distances obtained at the shorter delay are more reliable as demonstrated by the smaller R factor. Remarkably, the ^{3}MLCT structure optimized by DFT shows bond distances in excellent agreement with the XTA values and, moreover, the Ru–N1(bpy) bond shortening and the Ru–N53(py) bond lengthening is well predicted by the computational analysis of the excited state.

For each of the discussed time delays, Figure 4 shows the surface contour plots of the fit R-factor as a function of $R_{Ru–N1}$ and $R_{Ru–N53}$ and the best fit $\Delta\chi_{fit}(q,\tau)$ curves, corresponding to the R-factor surface global minimum. $\Delta\chi_{fit}(q,\tau)$ plots (magenta solid line) are superimposed on time-dependent differential $\Delta\chi_{exp}(q,\tau)$ spectra (black circles). The fit components relative to the ^{3}MLCT (blue solid line) and PHP (green solid line) contributions to the overall XTA signal are shown as well in Figure 4.

The $\Delta\chi_{exp}(q,\tau = 500$ ps) spectrum is optimally reproduced, as demonstrated by the very low R-factor value obtained (R = 0.180). Nevertheless, the corresponding R-factor surface shows an additional local minimum (R = 0.194) due to an inversion in the shortening and lengthening of the $R_{Ru–N1}$ and $R_{Ru–N53}$.[44] In the case of $\Delta\chi_{exp}(q,\tau = 3000$ ps), the amplitude of the differential spectrum is decreased approximately by a half with respect to 500 ps signal, resulting in a smaller signal-to-noise ratio. This is consistent with a reduced ^{3}MLCT population and causes an increase in the minimum R-factor found for such time delay (R = 0.378). Importantly, the ^{3}MLCT structural parameters found at 3000 ps are in good agreement with the values found at 500 ps, endorsing the stability of the refinement procedure adopted.

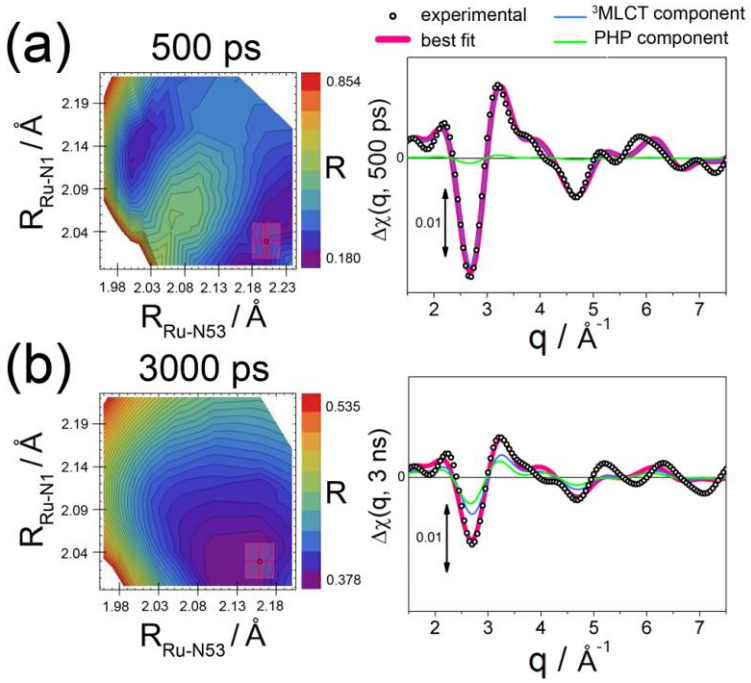

Figure 4. Surface contour plots of the fit R-factor as a function of $R_{Ru–N1}$ and $R_{Ru–N53}$ and best fit $\Delta\chi_{fit}(q,\tau)$ curves corresponding to the R-factor surface global minimum (magenta solid lines), superimposed to experimental TR-EXAFS data (black circles) for (a) τ = 500 ps and (b) τ = 3000 ps. The magenta box identifies the experimental error interval (± 0.02 Å on both $R_{Ru–N1}$ and $R_{Ru–N53}$ axis) around the minimum localized at the crossing point of the lines. The fit components relative to the ^{3}MLCT and PHP contributions to the overall TR-EXAFS signal are indicated as blue and green solid lines, respectively.

The XTA interpretation for the 150 ps delay requires a separate discussion. Analysis of the fitting results clearly gives the ^{3}MLCT state as the dominant structural component at 150 ps after laser excitation. The use of a different starting geometry, as for example the ^{3}MC, causes a ~50% increase in the R-factor (see SIC6). Compared to 500 ps and 3000 ps, a smaller distortion of ^{3}MLCT optimized bond distances, $R_{Ru–N1}$ = (2.07 ± 0.02) Å and $R_{Ru–N53}$ = (2.06 ± 0.02) Å, is found at 150 ps. Such a discrepancy is interpretable by the lack of a third structural component in the fitting model. The missing contribution is minor, but sufficient to perturb the XTA signal and can tentatively be ascribed to the ^{3}MC state and to the structural changes due to the photochemistry of the complex. XTA data acquired during this experiment are not suitable in terms of time-resolution and signal-to-noise ratio to allow a stable fit to be obtained in which a third minor structural component is isolated. In future work, improved statistics for measurements in the 50 ps−150 ps time-delay interval will be required if the elusive ^{3}MC state is to be detected and its structural rearrangements are to be determined.

CONCLUSIONS

Resolution of the excited state ^{3}MLCT structure was achieved by differential analysis of XTA data at 500 ps and 3000 ps after light excitation. These results are notable for the following reasons: 1) the

photoprocess is irreversible; 2) there are multiple contributions to the time dependent EXAFS signal; and 3) the close similarity between the GS and ^{3}MLCT structures of *cis*-$[Ru(bpy)_2(py)_2]^{2+}$.

Uniquely, XTA provides an experimental validation of the computed excited-state ^{3}MLCT structure, capturing the lengthening of one pyridine-ruthenium bond (Ru–N53) and the shortening of the ruthenium-nitrogen bond relative to the bpy ring *trans* to it (Ru–N1). Very small fluctuations in the Ru–N bond distances are found using various DFT functionals in the case of the ^{3}MLCT structure, confirming the robustness of this computational approach to investigate the excited states of metal complexes. Direct and experimental determination of the structure of the ^{3}MC state remains a challenging goal. However the present results indicate that such a state is the lowest-lying triplet excited state for *cis*-$[Ru(bpy)_2(py)_2]^{2+}$ and that DFT excited-state structures, including the ^{3}MC, can be reasonably calculated for Ru polypyridyl complexes. Importantly, accurate computational modeling of the lowest-lying triplet state can be effectively exploited as a diagnostic tool to predict the photoactivity of a metal complex before synthetic work is undertaken.

Finally, according to the interpretation of OTA and XTA data, the dissociation of the pyridine ligand is complete ca. 3 ns after light excitation.

MATERIAL AND METHODS

Sample preparation. *Cis*-$[Ru(bpy)_2(py)_2](ClO_4)_2$[45] and *cis*-$[Ru(bpy)_2(py)(H_2O)]ClO_4$[46] were synthesized according to literature procedures. To increase the water solubility, the chloride derivative *cis*-$[Ru(bpy)_2(py)_2]Cl_2$ was prepared by anion exchange of a methanol solution of *cis*-$[Ru(bpy)_2(py)_2](ClO_4)_2$ on a Dowex weakly basic anion exchanger resin (purchased from Aldrich).

Computational details. All calculations were performed with the Gaussian 09 (G09) program,[47] employing the DFT method. A range of functionals and basis sets were tested in the geometry optimization calculations of the GS, ^{3}MLCT, ^{3}MC and PHP and in the calculation of singlet and triplet transition energies by TDDFT. Full account of the methods and results is provided in the Supporting Information, SIA.

Optical transient absorption experimental details. Optical transient absorption measurements were performed at Center of Nanoscale Materials (CNM) of Argonne National Laboratory. The ultrafast TA system consists of a Ti:Sapphire regenerative amplified laser system with 1.7 kHz repetition rate and the output of Ti:Sapphire amplifier was split into two beams. The major part (95%) was used to pump to an optical parametric amplifier (OPA) to generate tunable pump pulse, while the rest was focused onto a sapphire disk to generate white light continuum probe. The white light was split into two beams that served as the reference and the probe respectively. The sample was excited using 390 nm pulses. The probe and pump beams were focused at the sample in a nearly collinear geometry to 0.3 mm and 0.1 mm diameter spots respectively, and with a "magic angle" of 54.7° in relative polarization directions. The transient absorption changes for a particular probe wavelength as a function of time were analyzed by fitting the data with a multiexponential kinetic model convoluted with a Gaussian instrument response function with 180 fs fwhm. The OTA spectra are chirp corrected to within 100 fs. The sample was prepared dissolving the complex *cis*-$[Ru(bpy)_2(py)_2]Cl_2$ in H_2O with the concentration of 0.2 mM. The sample cuvette path length was 2 mm. The pump power was 270 μW. A fluency of 0.003 J cm^{-2} was determined and the concentration of light-generated solvated electrons

was estimated to be under the detection limit using data available in the literature for $[Ru(bpy)_3]^{2+}$.[48] The sample damage was negligible during the OTA measurement based on UV-vis spectra measurement.

X-ray transient absorption experimental details. XTA measurements were carried out at the 11ID-D beamline of the Advanced Photon Source (APS), Argonne National Laboratory.[8, 9, 16, 49-52] The repetition rate of the laser pump/X-ray probe cycle was 1 kHz. The pump laser pulses were obtained from the output of a Nd/YLF laser (λ = 351 nm, 1 kHz repetition rate, 0.4 mJ/pulse and 5 ps fwhm). The laser fluency was determined to be 0.035 J cm^{-2} corresponding to an estimated concentration of light-generated solvated electrons < 2%.[48] The laser excitation energy well fits the absorption band of the *cis*-$[Ru(bpy)_2(py)_2]^{2+}$ centered at 338 nm (see absorption spectrum in Figure C1a). The experiment was conducted under standard operation mode of APS. The X-ray probe pulses (approximately 10^6 photons/pulse at 22 keV, 79 ps fwhm, 6.5 MHz) were extracted from a train of electron bunches circulating in the storage ring. Therefore, only 0.015% of total X-ray photons could effectively be used at 1 kHz repetition rate. The time delay between the laser and the X-ray pulses was adjusted by a programmable delay line (PDL-100A-20NS, Colby Instruments) based on a fast GaAs diode detector signal positioned at the sample location to detect both X-ray and laser pulses. The laser pump and the X-ray probe beams were overlapped at a continuously flowing jet of 1 mM aqueous *cis*-$[Ru(bpy)_2(py)_2]Cl_2$, of about 0.5 mm thickness. Two photomultiplier tubes (PMTs) coupled with plastic scintillators were used at 90˚ angles on both sides of the incident X-ray beam to collect the X-ray fluorescence signals. A soller slits/Zn filter combo was inserted between the sample fluid jet and the PMT detectors, which were custom-designed for the specific sample chamber configuration and the distance between the sample and the detector. The current mode of the PMTs was used in order to acquire multiple photons from each X-ray pulse as the flux of the X-ray photons exceeded significantly the single photon counting limit. The outputs of the PMTs were sent to two fast analyzer cards (Agilent) that were triggered by a signal at 1 kHz from the scattered laser light collected by a photo diode. The card digitized the X-ray fluorescence signals as a function of time at 1ns/point after each trigger. The process was repeated and integrated for 4 s at each energy point for each scan. The fast detect and data collection systems allow collection of all X-ray pulses between two laser pulses with resolution of individual X-ray pulses. A real-time data processing software was implemented to extract the signal amplitude of each X-ray pulse.

Available Supporting Information. A) Full description of DFT methods and results; B) full description of transient absorption results and data analysis; C) full description of XTA experimental setup and data reduction and analysis.

ACKNOWLEDGMENTS

LS was supported for this work by Marie Curie Intraeuropean Fellowship (220281 PHOTORUACD) and by European Research Council (ERC) BIO-INCMED (PJS). Use of the APS and the CNM is supported by DOE-BES under Contract No. DE-AC02-06CH11357. LS gratefully acknowledges the MICINN of Spain for the Ramón y Cajal Fellowship RYC-2011-07787. The authors are grateful to the APS for GUP 12873 and to M. Castagna and Fratelli Castagna s.r.l. for a generous travel funding to CG and TR.

REFERENCES

1. L. X. Chen, *Angew. Chem. Int. Ed.*, 2004, **43**, 2886-2905.
2. C. Bressler and M. Chergui, *Chem. Rev.*, 2004, **104**, 1781-1812.
3. H. Ihee, *Acc. Chem. Res.*, 2009, **42**, 356-366.
4. H. Ihee, M. Lorenc, T. K. Kim, Q. Y. Kong, M. Cammarata, J. H. Lee, S. Bratos and M. Wulff, *Science*, 2005, **309**, 1223-1227.
5. C. Bressler, C. Milne, V. T. Pham, A. El Nahhas, R. M. van der Veen, W. Gawelda, S. Johnson, P. Beaud, D. Grolimund, M. Kaiser, C. N. Borca, G. Ingold, R. Abela and M. Chergui, *Science*, 2009, **323**, 489-492.
6. F. Schotte, M. H. Lim, T. A. Jackson, A. V. Smirnov, J. Soman, J. S. Olson, G. N. Phillips, M. Wulff and P. A. Anfinrud, *Science*, 2003, **300**, 1944-1947.
7. A. B. Wohri, G. Katona, L. C. Johansson, E. Fritz, E. Malmerberg, M. Andersson, J. Vincent, M. Eklund, M. Cammarata, M. Wulff, J. Davidsson, G. Groenhof and R. Neutze, *Science*, 2003, **328**, 630-633.
8. L. X. Chen, in *Annu. Rev. Phys. Chem.*, 2005, vol. 56, pp. 221-254.
9. L. X. Chen, W. J. H. Jager, G. Jennings, D. J. Gosztola, A. Munkholm and J. P. Hessler, *Science*, 2001, **292**, 262-264.
10. L. X. Chen, X. Y. Zhang, E. C. Wasinger, K. Attenkofer, G. Jennings, A. Z. Muresan and J. S. Lindsey, *J. Am. Chem. Soc.*, 2007, **129**, 9616-9618.
11. L. X. Chen, X. Y. Zhang, E. C. Wasinger, J. V. Lockard, A. B. Stickrath, M. W. Mara, K. Attenkofer, G. Jennings, G. Smolentsev and A. Soldatov, *Chem. Sci.*, 2010, **1**, 642-650.
12. W. Gawelda, M. Johnson, F. M. F. de Groot, R. Abela, C. Bressler and M. Chergui, *J. Am. Chem. Soc.*, 2006, **128**, 5001-5009.
13. W. Gawelda, V. T. Pham, M. Benfatto, Y. Zaushitsyn, M. Kaiser, D. Grolimund, S. L. Johnson, R. Abela, A. Hauser, C. Bressler and M. Chergui, *Phys. Rev. Lett.*, 2007, **98**, 057401.
14. L. X. Chen, G. B. Shaw, I. Novozhilova, T. Liu, G. Jennings, K. Attenkofer, G. J. Meyer and P. Coppens, *J. Am. Chem. Soc.*, 2003, **125**, 7022-7034.
15. R. M. van der Veen, C. J. Milne, A. El Nahhas, F. A. Lima, V. T. Pham, J. Best, J. A. Weinstein, C. N. Borca, R. Abela, C. Bressler and M. Chergui, *Angew. Chem. Int. Ed.*, 2009, **48**, 2711-2714.
16. J. V. Lockard, A. A. Rachford, G. Smolentsev, A. B. Stickrath, X. H. Wang, X. Y. Zhang, K. Atenkoffer, G. Jennings, A. Soldatov, A. L. Rheingold, F. N. Castellano and L. X. Chen, *J. Phys. Chem. A*, 2010, **114**, 12780-12787.
17. S. Cho, M. W. Mara, X. Wang, J. V. Lockard, A. A. Rachford, F. N. Castellano and L. X. Chen, *J. Phys. Chem. A*, 2011, **115**, 3990-3996.
18. D. Gust, T. A. Moore and A. L. Moore, *Acc. Chem. Res.*, 2009, **42**, 1890-1898.
19. T. S. Teets and D. G. Nocera, *Chem. Commun.*, 2011, **47**, 9268-9274.
20. R. E. Blankenship, *Molecular Mechanisms of Photosynthesis*, Blackwell Science, Oxford, 2002.
21. N. J. Farrer, L. Salassa and P. J. Sadler, *Dalton Trans.*, 2009, 10690-10701.
22. S. Betanzos-Lara, L. Salassa, A. Habtemariam, O. Novakova, A. M. Pizarro, G. J. Clarkson, B. Liskova, V. Brabec and P. J. Sadler, *Organometallics*, 2012, **31**, 3466-3479.
23. S. Betanzos-Lara, L. Salassa, A. Habtemariam and P. J. Sadler, *Chem. Commun.*, 2009, 6622-6624.
24. F. Barragan, P. Lopez-Senin, L. Salassa, S. Betanzos-Lara, A. Habtemariam, V. Moreno, P. J. Sadler and V. Marchan, *J. Am. Chem. Soc.*, 2011, **133**, 14098-14108.
25. L. Zayat, C. Calero, P. Albores, L. Baraldo and R. Etchenique, *J. Am. Chem. Soc.*, 2003, **125**, 882-883.
26. T. Respondek, R. N. Garner, M. K. Herroon, I. Podgorski, C. Turro and J. J. Kodanko, *J. Am. Chem. Soc.*, 2011, **133**, 17164-17167.
27. J. V. Caspar and T. J. Meyer, *Inorg. Chem.*, 1983, **22**, 2444-2453.
28. W. M. Wacholtz, R. A. Auerbach, R. H. Schmehl, M. Ollino and W. R. Cherry, *Inorg. Chem.*, 1985, **24**, 1758-1760.

29. M. Adelt, M. Devenney, T. J. Meyer, D. W. Thompson and J. A. Treadway, *Inorg. Chem.*, 1998, **37**, 2616-2617.
30. F. Barigelletti, A. Juris, V. Balzani, P. Belser and A. Von Zelewsky, *J. Phys. Chem.*, 1987, **91**, 1095-1098.
31. P. S. Wagenknecht and P. C. Ford, *Coord. Chem. Rev.*, 2011, **255**, 591-616.
32. B. Durham, J. V. Caspar, J. K. Nagle and T. J. Meyer, *J. Am. Chem. Soc.*, 1982, **104**, 4803-4810.
33. D. W. Thompson, C. N. Fleming, B. D. Myron and T. J. Meyer, *J. Phys. Chem. B*, 2007, **111**, 6930-6941.
34. L. Salassa, C. Garino, G. Salassa, R. Gobetto and C. Nervi, *J. Am. Chem. Soc.*, 2008, **130**, 9590-9597.
35. T. Osterman, M. Abrahamsson, H. C. Becker, L. Hammarstrom and P. Persson, *J. Phys. Chem. A*, 2012, **116**, 1041-1050.
36. L. Salassa, E. Borfecchia, T. Ruiu, C. Garino, D. Gianolio, R. Gobetto, P. J. Sadler, M. Cammarata, M. Wulff and C. Lamberti, *Inorg. Chem.*, 2010, **49**, 11240-11248.
37. J. K. McCusker, *Acc. Chem. Res.*, 2003, **36**, 876-887.
38. Y. Liu, D. B. Turner, T. N. Singh, A. M. Angeles-Boza, A. Chouai, K. R. Dunbar and C. Turro, *J. Am. Chem. Soc.*, 2009, **131**, 26-27.
39. S. Wallin, J. Davidsson, J. Modin and L. Hammarstrom, *J. Phys. Chem. A*, 2005, **109**, 4697-4704.
40. M. O. Krause and J. H. Oliver, *J. Phys. Chem. Ref. Data*, 1979, **8**, 329-338.
41. A Fourier filtering procedure was applied to raw $\Delta\chi(k,\tau)$ curves: the EXAFS signal was first Fourier transformed from k- to R-space using the k range 2.5 $Å^{-1}$ – 10.8 $Å^{-1}$, and then only the R-range 1.0 Å – 5.0 Å, where an effectively physical signal is expected, is back-Fourier transformed into momentum space, named q-space to be distinguished from the starting k-space (more details in SIC2).
42. L. Salassa, D. Gianolio, C. Garino, G. Salassa, E. Borfecchia, T. Ruiu, C. Nervi, R. Gobetto, R. Bizzarri, P. J. Sadler and C. Lamberti, *J. Phys.: Conf. Ser.*, 2009, **190**, 012141.
43. L. Salassa, T. Ruiu, C. Garino, A. M. Pizarro, F. Bardelli, D. Gianolio, A. Westendorf, P. J. Bednarski, C. Lamberti, R. Gobetto and P. J. Sadler, *Organometallics*, 2010, **29**, 6703-6710.
44. The presence of two minima is not surprising since EXAFS is not able to discriminate between a pyridine ring and a single ring in a bpy unit. A similar case was found in the PHP structure refinement and full discussion is provided in the Supporting Information (SIC5).
45. F. P. Dwyer, H. A. Goodwin and E. C. Gyarfas, *Aust. J. Chem.*, 1963, **16**, 544-548.
46. X. Hua and A. G. Lappin, *Inorg. Chem.*, 1995, **34**, 992-994.
47. M. J. Frisch, G. W. Trucks, H. B. Schlegel, G. E. Scuseria, M. A. Robb, J. R. Cheeseman, G. Scalmani, V. Barone, B. Mennucci, G. A. Petersson, H. Nakatsuji, M. Caricato, X. Li, H. P. Hratchian, A. F. Izmaylov, J. Bloino, G. Zheng, J. L. Sonnenberg, M. Hada, M. Ehara, K. Toyota, R. Fukuda, J. Hasegawa, M. Ishida, T. Nakajima, Y. Honda, O. Kitao, H. Nakai, T. Vreven, J. Montgomery, J. A., J. E. Peralta, F. Ogliaro, M. Bearpark, J. J. Heyd, E. Brothers, K. N. Kudin, V. N. Staroverov, R. Kobayashi, J. Normand, K. Raghavachari, A. Rendell, J. C. Burant, S. S. Iyengar, J. Tomasi, M. Cossi, N. Rega, N. J. Millam, M. Klene, J. E. Knox, J. B. Cross, V. Bakken, C. Adamo, J. Jaramillo, R. Gomperts, R. E. Stratmann, O. Yazyev, A. J. Austin, R. Cammi, C. Pomelli, J. W. Ochterski, R. L. Martin, K. Morokuma, V. G. Zakrzewski, G. A. Voth, P. Salvador, J. J. Dannenberg, S. Dapprich, A. D. Daniels, Ö. Farkas, J. B. Foresman, J. V. Ortiz, J. Cioslowski and D. J. Fox, Gaussian, Inc., Wallingford, CT, Revision A.1 edn., 2009.
48. A. N. Tarnovsky, W. Gawelda, M. Johnson, C. Bressler and M. Chergui, *J. Phys. Chem. B*, 2006, **110**, 26497-26505.
49. L. X. Chen, G. Jennings, T. Liu, D. J. Gosztola, J. P. Hessler, D. V. Scaltrito and G. J. Meyer, *J. Am. Chem. Soc.*, 2002, **124**, 10861-10867.
50. G. Jennings, W. J. H. Jager and L. X. Chen, *Rev. Sci. Instrum.*, 2002, **73**, 362-368.
51. L. X. Chen, X. Y. Zhang, J. V. Lockard, A. B. Stickrath, K. Attenkofer, G. Jennings and D. J. Liu, *Acta Crystallogr. Sect. A*, 2010, **66**, 240-251.
52. X. Y. Zhang, G. Smolentsev, J. C. Guo, K. Attenkofer, C. Kurtz, G. Jennings, J. V. Lockard, A. B. Stickrath and L. X. Chen, *J. Phyis. Chem. Lett.*, 2011, **2**, 628-632.

Supporting Information

X-Ray Transient Absorption Structural Characterization of the ^{3}MLCT Triplet Excited State of *cis*-$[Ru(bpy)_2(py)_2]^{2+}$

Elisa Borfecchia,[a] Claudio Garino,[a] Luca Salassa,*[‡b] Tiziana Ruiu,[a] Diego Gianolio,[c] Xiaoyi Zhang,[d] Klaus Attenkofer,[d] Lin X. Chen,[d,e] Roberto Gobetto,[a] Peter. J. Sadler,[b] and Carlo Lamberti*[a]

[a] Department of Chemistry and NIS Centre of Excellence, University of Turin via P. Giuria 7, 10125 Turin (Italy)

[b] Department of Chemistry, University of Warwick Gibbet Hill Rd, Coventry CV4 7AL (UK)

[c] Diamond Light Source Ltd., Harwell Science and Innovation Campus, OX11 0DE Didcot (UK)

[d] X-ray Science Division and Chemical Sciences & Engineering Division, Argonne National Laboratory 9700 South Cass Ave., Argonne, IL 60439 (USA)

[e] Department of Chemistry, Northwestern University 2145 Sheridan Road, Evanston, IL 60208 (USA)

[‡] Current address: CIC biomaGUNE, Paseo Miramón 182, 20009 Donostia–San Sebastian (Spain)

Table of Contents of the Supporting Information

A – Computational Data

A1. Computational details

All calculations were performed with the Gaussian 09 (G09) program,[1] employing the DFT method. For *cis*-$[Ru(bpy)_2(py)_2]^{2+}$, the singlet ground state (GS) geometry and the triplet geometries corresponding to a ^{3}MLCT and ^{3}MC state (lowest-lying) were fully optimized with the B3LYP[2, 3] and PBE0[4, 5] functionals at either the LanL2DZ/6-31+G** or LanL2DZ/6-311G** level.[6, 7] Triplet geometries were obtained using the unrestricted Kohn-Sham formalism (UKS).[8] In the case of the photoproduct *cis*-$[Ru(bpy)_2(py)(H_2O)]^{2+}$, only the singlet ground state geometry was optimized with the same functionals and basis sets. All optimizations were performed including the solvent effect (CPCM method)[9-11] with water or dichloromethane as solvent. The ^{3}MC state geometry of *cis*-$[Ru(bpy)_2(py)_2]^{2+}$ computed at the B3LYP/LanL2DZ/6-31+G** level could not be optimized with the CPCM solvent model. Only for this case we performed the geometry optimization in the gas phase. The nature of all stationary points was confirmed by normal-mode analysis. A set of other six functionals (TPSSh,[1212] M06,[13] mPW1PBE, mPW1LYP,[14] m062X,[13] HSEh1PBE[15]) was tested as well for the optimization of the ^{3}MLCT and ^{3}MC geometries of *cis*-$[Ru(bpy)_2(py)_2]^{2+}$.

Fifty singlet-singlet electronic transitions were calculated by TDDFT,[16, 17] employing the ground state structures optimized with the B3LYP and PBE0 functionals together with the LanL2DZ/6-31+G** and LanL2DZ/6-311G** basis sets. The same methods were adopted to calculate four singlet-triplet electronic transitions from the ^{3}MLCT and ^{3}MC state geometries, while sixteen triplet-triplet transitions were calculated from the same triplet geometries by TDDFT/PBE0/LanL2DZ/6-311G** to aid the assignment of the transient absorption experiment. Solvent effects were considered using the CPCM method and water as solvent. The program GaussSum 1.05[18] was adopted to simulate the electronic spectra of the ruthenium complex and to visualize the singlet excited state transitions as electron density difference maps (EDDMs). Computational results are summarized in the tables and graphics below.

Molecular graphics images were produced using the UCSF Chimera package from the Resource for Biocomputing, Visualization, and Informatics at the University of California, San Francisco (supported by NIH P41 RR001081).[19]

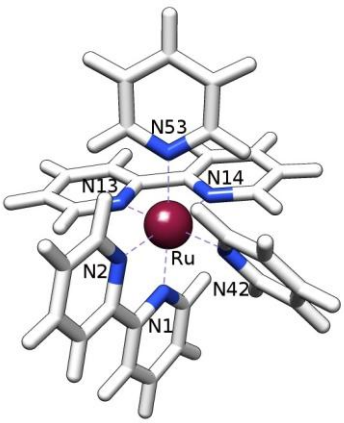

Scheme A1. Atom-numbering scheme for complex *cis*-$[Ru(bpy)_2(py)_2]^{2+}$.

A2. Geometry optimizations

Table A1. Calculated bond lengths for the singlet ground state (GS) and triplet ^{3}MLCT and ^{3}MC states of *cis*-$[Ru(bpy)_2(py)_2]^{2+}$ in water. Solvent effects were included using the CPCM method. The LanL2DZ ECP was employed for the Ru atom in all calculations.

Bond lengths – GS						
	Ru–N1(bpy)	**Ru–N2(bpy)**	**Ru–N13(bpy)**	**Ru–N14(bpy)**	**Ru–N42(py)**	**Ru–N53(py)**
B3LYP/ 6-31+G**	2.10259	2.12146	2.10257	2.12145	2.17384	2.17382
B3LYP/ 6-311G**	2.10464	2.12287	2.10464	2.12286	2.17518	2.17517
PBE0/ 6-31+G**	2.07556	2.09187	2.07556	2.09186	2.13571	2.13570
PBE0/ 6-311G**	2.07627	2.09209	2.07627	2.09208	2.13559	2.13558
Average	2.08976	2.10707	2.08976	2.10706	2.15508	2.15507
Bond lengths – ^{3}MLCT						
	Ru–N1(bpy)	**Ru–N2(bpy)**	**Ru–N13(bpy)**	**Ru–N14(bpy)**	**Ru–N42(py)**	**Ru–N53(py)**
B3LYP/ 6-31+G**	2.03755	2.08232	2.09092	2.14513	2.17467	2.21023
B3LYP/ 6-311G**	2.04618	2.08438	2.09443	2.14586	2.17739	2.20936
PBE0/ 6-31+G**	2.06639	2.11384	2.02104	2.05892	2.17129	2.13942
PBE0/ 6-311G**	2.02713	2.06077	2.06827	2.11325	2.14076	2.16950
TPSSh/ 6-311G**	2.03809	2.06718	2.07935	2.12008	2.14749	2.17310
M06/ 6-311G**	2.05237	2.07297	2.08410	2.13411	2.15277	2.18739
mPW1PBE/ 6-311G**	2.02693	2.06111	2.06844	2.11364	2.14152	2.17041
mPW1LYP/ 6-311G**	2.04627	2.08651	2.09498	2.14803	2.17784	2.21079
m062X/ 6-311G**	2.03792	2.07337	2.08753	2.14808	2.15756	2.19219
HSEh1PBE/ 6-311G**	2.03016	2.06476	2.07205	2.11763	2.14345	2.17192
Average	2.04090	2.07672	2.07611	2.12447	2.15847	2.18343
Bond lengths – ^{3}MC						
	Ru–N1(bpy)	**Ru–N2(bpy)**	**Ru–N13(bpy)**	**Ru–N14(bpy)**	**Ru–N42(py)**	**Ru–N53(py)**
B3LYP/ 6-31+G**	n.d.	n.d.	n.d.	n.d.	n.d.	n.d.
B3LYP/ 6-311G**	2.39654	2.19274	2.11545	2.11600	2.16988	3.05937
PBE0/ 6-31+G**	2.37337	2.16741	2.09550	2.09018	2.13560	2.76960
PBE0/ 6-311G**	2.36813	2.16202	2.09710	2.09354	2.14162	2.80235
TPSSh/ 6-311G**	2.35651	2.16621	2.09708	2.09377	2.15467	2.86803
M06/ 6-311G**	2.36324	2.17640	2.11450	2.11181	2.13707	2.79295
mPW1PBE/	2.36738	2.15829	2.09456	2.09189	2.14640	2.88357

6-311G**						
mPW1LYP/ 6-311G**	2.39910	2.19344	2.12421	2.11789	2.16665	3.16614
m062X/ 6-311G**	2.41366	2.22839	2.13711	2.13724	2.16186	2.78585
HSEh1PBE/ 6-311G**	2.37321	2.16988	2.10093	2.09740	2.14301	2.76736
Average	2.37902	2.17942	2.10849	2.10552	2.15075	2.87725

n.d.= not determined. All our attempts to optimize the ^{3}MC geometry at the B3LYP/6-31+G** with the CPCM solvent model were not successful.

Table A2. Calculated bond lengths for the singlet ground state (GS) of *cis*-$[Ru(bpy)_2(py)(H_2O)]^{2+}$ (PHP) in water. Solvent effects were included using the CPCM method. The LanL2DZ ECP was employed for the Ru atom in all calculations.

Bond lengths – GS						
	Ru–N1(bpy)	**Ru–N2(bpy)**	**Ru–N13(bpy)**	**Ru–N14(bpy)**	**Ru–N42(py)**	**Ru–O53(H_2O)**
B3LYP/ 6-31+G**	2.05793	2.10717	2.09799	2.11866	2.16651	2.23388
B3LYP/ 6-311G**	2.06486	2.09824	2.10413	2.12030	2.16455	2.23856
PBE0/ 6-31+G**	2.03071	2.08070	2.07180	2.08992	2.12946	2.20497
PBE0/ 6-311G**	2.03721	2.07069	2.07660	2.09148	2.12792	2.20723
Average	2.04768	2.08920	2.08763	2.10509	2.14711	2.22116

Table A3. Calculated bond lengths for the triplet ^{3}MLCT and ^{3}MC states of *cis*-$[Ru(bpy)_2(py)_2]^{2+}$ in dichloromethane. Solvent effects were included using the CPCM method. The LanL2DZ ECP was employed for the Ru atom in all calculations.

Bond lengths – ^{3}MLCT						
	Ru–N1(bpy)	**Ru–N2(bpy)**	**Ru–N13(bpy)**	**Ru–N14(bpy)**	**Ru–N42(py)**	**Ru–N53(py)**
PBE0/ 6-311G**	2.02522	2.05937	2.06919	2.11496	2.14086	2.17135
TPSSh/ 6-311G**	2.03689	2.06618	2.08011	2.12138	2.14739	2.17404
M06/ 6-311G**	2.05241	2.07227	2.08514	2.13664	2.15281	2.19068
m062X/ 6-311G**	2.03586	2.07152	2.08860	2.15082	2.15768	2.19478
Average	2.03760	2.06734	2.08076	2.13095	2.14968	2.18271
Bond lengths – ^{3}MC						
	Ru–N1(bpy)	**Ru–N2(bpy)**	**Ru–N13(bpy)**	**Ru–N14(bpy)**	**Ru–N42(py)**	**Ru–N53(py)**
PBE0/ 6-311G**	2.36858	2.16506	2.09731	2.09274	2.13807	2.77434
TPSSh/ 6-311G**	2.35850	2.16755	2.10271	2.09323	2.14729	2.80889
M06/ 6-311G**	2.36446	2.17650	2.11528	2.11160	2.13665	2.77980
m062X/ 6-311G**	2.41584	2.22738	2.13854	2.13683	2.15991	2.76488
Average	2.37685	2.18412	2.11346	2.10860	2.14548	2.78198

A3. TDDFT electronic transitions

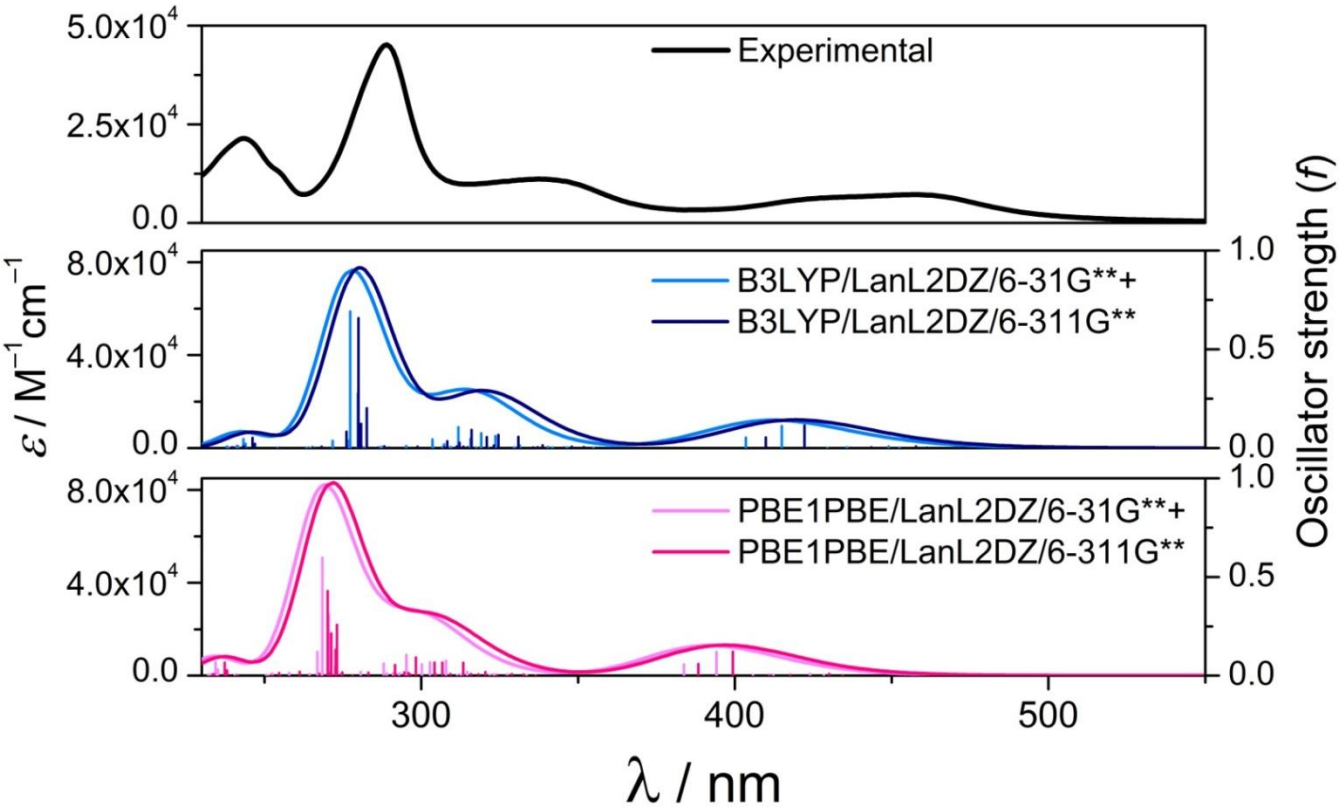

Figure A1. Experimental (black line) and calculated (colored lines) absorption spectra of *cis*-$[Ru(bpy)_2(py)_2]^{2+}$ in water. The singlet excited transitions are shown as vertical bars with heights equal to the extinction coefficients. The theoretical curve was obtained using the program GAUSSSUM 1.05.

Table A4. Selected TDDFT singlet-singlet transitions and corresponding electron difference density maps (EDDMs) for *cis*-$[Ru(bpy)_2(py)_2]^{2+}$ in water at the B3LYP/LanL2DZ/6-31+G** level. In the EDDMs light blue indicates a decrease in electron density, while dark blue indicates an increase.

Tr.	E_{calc}, eV (nm)	*f*	Composition	Character	EDDMs
5	2.9879 (414.95)	0.1122	H-2→L+1 (76%) H-1→LUMO (18%)	MLCT (Ru→bpy)	
6	3.0727 (403.51)	0.0528	H-2→LUMO (53%) H-1→L+1 (30%)	MLCT (Ru→bpy)	
12	3.7418 (331.35)	0.0134	H-2→L+2 (11%) H-1→L+3 (65%) HOMO→L+4 (15%)	MLCT (Ru→py)	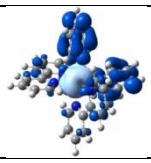
15	3.8309	0.0608	H-2→L+2 (83%)	MLCT	

	(323.64)			(Ru→bpy)	
17	3.8849 (319.14)	0.0748	H-2→L+3 (10%) H-1→L+4 (31%) HOMO→L+5 (11%) HOMO→L+7 (26%)	MLCT (Ru→py/bpy)	
19	3.9270 (315.72)	0.0471	H-2→L+4 (77%) H-1→L+7 (7%)	MLCT (Ru→py)	
20	3.9766 (311.78)	0.1056	HOMO→L+6 (78%)	MLCT (Ru→bpy)	
23	4.0346 (307.3)	0.0189	H-1→L+5 (69%) H-1→L+7 (13%)	MLCT (Ru→bpy)	
26	4.0842 (303.57)	0.0437	H-2→L+5 (54%) H-2→L+7 (37%)	MLCT (Ru→bpy)	
27	4.2003 (295.18)	0.0103	H-1→L+6 (14%) H-1→L+10 (18%) HOMO→L+8 (27%) HOMO→L+11 (23%)	MLCT (Ru→py/bpy)	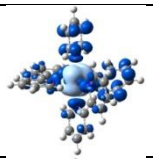
35	4.4320 (279.75)	0.2771	H-4→LUMO (35%) H-3→L+1 (34%)	LC (bpy) + MLCT (Ru→bpy)	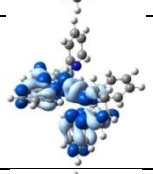
36	4.4710 (277.31)	0.6917	H-4→L+1 (42%) H-3→LUMO (29%) H-2→L+6 (9%)	MLCT (Ru→bpy)	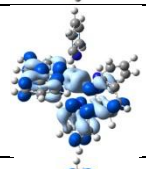
37	4.4763 (276.98)	0.0398	H-2→L+8 (63%) H-2→L+11 (13%)	MLCT (Ru→py)	
38	4.5631 (271.71)	0.0373	HOMO→L+9 (96%)	MLCT (Ru→py)	
45	5.0822 (243.96)	0.0219	H-3→L+2 (78%)	LC (bpy)	
46	5.0963 (243.28)	0.0462	H-4→L+2 (60%) H-3→L+3 (26%)	LC/IL (bpy→py)	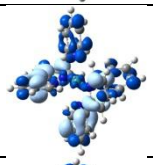
48	5.1397 (241.23)	0.0111	H-4→L+3 (55%) H-3→L+4 (14%)	IL (bpy→py)	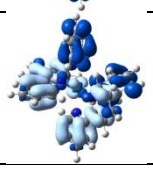

f = oscillator strength

Table A5. Selected TDDFT singlet-singlet transitions and corresponding electron difference density maps (EDDMs) for *cis*-$[Ru(bpy)_2(py)_2]^{2+}$ in water at the B3LYP/LanL2DZ/6-311G** level. In the EDDMs light blue indicates a decrease in electron density, while dark blue indicates an increase.

Tr.	E_{calc}, eV (nm)	*f*	Composition	Character	EDDMs
5	2.9368 (422.18)	0.1136	H-2→LUMO (77%) H-1→L+1 (18%)	MLCT (Ru→bpy)	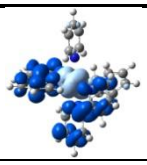
6	3.0250 (409.86)	0.0536	H-2→L+1 (55%) H-1→LUMO (29%) HOMO→L+1 (11%)	MLCT (Ru→bpy)	
12	3.6604 (338.71)	0.0142	H-2→L+2 (10%) H-1→L+3 (74%) HOMO→L+4 (9%)	MLCT (Ru→py)	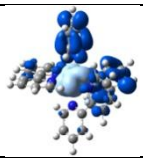
15	3.7464 (330.95)	0.057	H-2→L+2 (82%)	MLCT (Ru→bpy)	
17	3.8198 (324.59)	0.0671	H-1→L+4 (35%) HOMO→L+5 (29%) HOMO→L+7 (16%)	MLCT (Ru→py/bpy)	
18	3.8370 (323.13)	0.013	H-2→L+3 (12%) HOMO→L+5 (57%) HOMO→L+7 (21%)	MLCT (Ru→bpy/py)	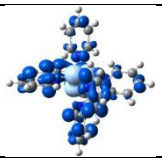
19	3.8637 (320.90)	0.0565	H-2→L+4 (80%)	MLCT (Ru→py)	
20	3.9231 (316.04)	0.0924	H-1→L+7 (-11%) HOMO→L+6 (74%)	MLCT (Ru→bpy)	
23	3.9713 (312.20)	0.0268	H-1→L+5 (39%) H-1→L+7 (34%), H-2→L+10 (7%) HOMO→L+6 (9%)	MLCT (Ru→bpy)	
25	4.0216 (308.29)	0.0348	H-2→L+5 (39%) H-2→L+7 (53%)	MLCT (Ru→bpy)	
35	4.3867 (282.64)	0.2016	H-4→L+1 (26%) H-3→LUMO (25%) H-2→L+8 (15%)	LC (bpy) + MC	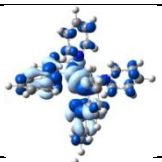
36	4.4152 (280.81)	0.1228	H-4→L+1 (16%) H-3→LUMO (12%) H-2→L+8 (42%) H-2→L+11 (10%)	MLCT (Ru→py)	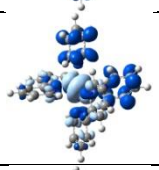
37	4.4286 (279.96)	0.6576	H-4→LUMO (42%) H-3→L+1 (28%)	LC (bpy) + MLCT (Ru→bpy)	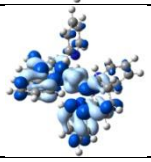

38	4.4906 (276.10)	0.0831	HOMO→L+9 (91%)	MLCT (Ru→py)	
45	5.0212 (246.92)	0.0224	H-3→L+2 (79%)	LC (bpy)	
46	5.0370 (246.15)	0.0521	H-4→L+2 (68%) H-3→L+3 (18%)	LC/IL (bpy→py)	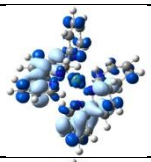
48	5.0972 (243.24)	0.0093	H-4→L+3 (61%) H-3→L+4 (13%)	IL (bpy→py)	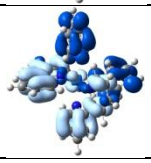

f = oscillator strength

Table A6. Selected TDDFT singlet-singlet transitions and corresponding electron difference density maps (EDDMs) for *cis*-$[Ru(bpy)_2(py)_2]^{2+}$ in water at the PBE0/LanL2DZ/6-31+G** level. In the EDDMs light blue indicates a decrease in electron density, while dark blue indicates an increase.

Tr.	**E_{calc}**, eV (nm)	***f***	**Composition**	**Character**	**EDDMs**
5	3.1459 (394.11)	0.1197	H-2→L+1 (73%) H-1→LUMO (19%)	MLCT (Ru→bpy)	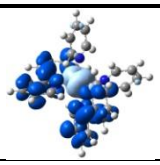
6	3.2309 (383.74)	0.0573	H-2→LUMO (44%) H-1→L+1 (36%) HOMO→LUMO (15%)	MLCT (Ru→bpy)	
12	3.9408 (314.62)	0.0181	H-2→L+2 (12%) H-1→L+3 (73%)	MLCT (Ru→py)	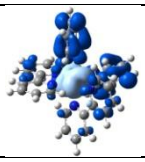
15	4.0267 (307.90)	0.0754	H-2→L+2 (78%)	MLCT (Ru→bpy)	
17	4.0955 (302.73)	0.0667	H-1→L+4 (57%) HOMO→L+7 (18%)	MLCT (Ru→py)	
19	4.1305 (300.17)	0.0573	H-2→L+4 (75%)	MLCT (Ru→py)	
20	4.1988 (295.28)	0.1047	HOMO→L+6 (77%)	MLCT (Ru→bpy)	
21	4.2313 (293.02)	0.0111	H-1→L+6 (60%) HOMO→L+7 (13%)	MLCT (Ru→bpy)	
24	4.2608 (290.99)	0.0109	H-1→L+5 (67%) H-1→L+7 (14%)	MLCT (Ru→bpy)	
25	4.2894 (289.04)	0.0106	H-2→L+6 (71%)	MLCT (Ru→bpy)	
26	4.3050 (288.00)	0.0611	H-2→L+5 (54%) H-2→L+7 (33%)	MLCT (Ru→bpy)	

27	4.4177 (280.65)	0.0181	H-1→L+6 (13%) H-1→L+11 (14%) HOMO→L+8 (24%) HOMO→L+12 (23%)	MLCT (Ru→py/bpy)	
32	4.5706 (271.27)	0.0525	H-4→L+1 (25%) H-3→LUMO (60%)	LC (bpy) + MC	
33	4.5839 (270.48)	0.3116	H-4→LUMO (28%) H-3→L+1 (32%)	LC (bpy) + MC	
34	4.6188 (268.43)	0.5983	H-4→L+1 (49%) H-3→LUMO (11%) H-2→L+6 (10%)	LC (bpy) + MC	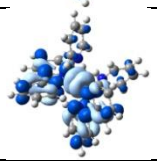
36	4.6457 (266.88)	0.1201	H-1→L+8 (83%)	MLCT (Ru→py)	
38	4.8081 (257.87)	0.0140	HOMO→L+9 (97%)	MLCT (Ru→py)	
39	4.9105 (252.49)	0.0111	H-5→LUMO (63%) H-2→L+9 (26%)	M(L)LCT (Ru(py)→bpy)	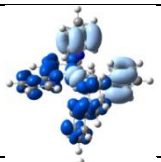
45	5.2721 (235.17)	0.0301	H-3→L+2 (73%)	LC (bpy)	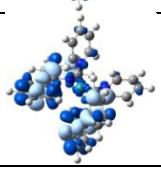
46	5.2892 (234.41)	0.0680	H-4→L+2 (67%)	LC (bpy)	

f = oscillator strength

Table A7. Selected TDDFT singlet-singlet transitions and corresponding electron difference density maps (EDDMs) for *cis*-$[Ru(bpy)_2(py)_2]^{2+}$ in water at the PBE0/LanL2DZ/6-311G** level. In the EDDMs light blue indicates a decrease in electron density, while dark blue indicates an increase.

Tr.	**E_{calc}**, eV (nm)	***f***	**Composition**	**Character**	
5	3.1045 (399.37)	0.1215	H-2→L+1 (73%) H-1→LUMO (19%)	MLCT (Ru→bpy)	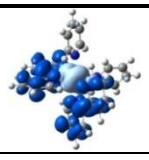
6	3.1929 (388.31)	0.0586	H-2→LUMO (45%) H-1→L+1 (35%) HOMO→LUMO (14%)	MLCT (Ru→bpy)	

12	3.8694 (320.42)	0.0185	H-2→L+2 (12%) H-1→L+3 (76%)	MLCT (Ru→py)	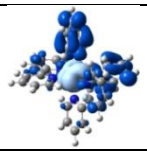
15	3.9566 (313.36)	0.0650	H-2→L+2 (66%)	MLCT (Ru→bpy)	
17	4.0426 (306.69)	0.0658	H-1→L+4 (54%) HOMO→L+5 (14%) HOMO→L+7 (15%)	MLCT (Ru→py)	
19	4.0759 (304.19)	0.0658	H-2→L+4 (77%)	MLCT (Ru→py)	
20	4.1564 (298.30)	0.0921	H-1→L+7 (10%) HOMO→L+6 (73%)	MLCT (Ru→bpy)	
22	4.1901 (295.90)	0.0131	H-2→L+5 (17%) H-1→L+6 (43%) HOMO→L+7 (13%)	MLCT (Ru→bpy)	
24	4.2087 (294.59)	0.0157	H-1→L+5 (43%) H-1→L+7 (33%)	MLCT (Ru→bpy)	
25	4.2499 (291.73)	0.0102	H-2→L+6 (76%)	MLCT (Ru→bpy)	
26	4.2514 (291.63)	0.0541	H-2→L+5 (44%) H-2→L+7 (43%)	MLCT (Ru→bpy)	
27	4.3794 (283.11)	0.0148	H-1→L+6 (13%) H-1→L+11 (11%) HOMO→L+8 (33%) HOMO→L+12 (18%)	MLCT (Ru→py/bpy)	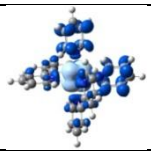
29	4.5113 (274.83)	0.0163	H-2→L+8 (15%) H-1→L+11 (24%) HOMO→L+8 (17%)	MLCT (Ru→py/bpy)	
31	4.5399 (273.10)	0.2579	H-3→L+1 (55%) HOMO→L+8 (14%)	LC (bpy) + MLCT (Ru→py)	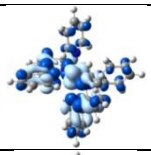
32	4.5468 (272.69)	0.1317	H-4→L+1 (14%) H-3→LUMO (71%)	LC (bpy) + MC	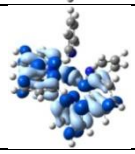
33	4.5478 (272.63)	0.0461	H-4→LUMO (67%) H-3→L+1 (18%)	LC (bpy) + MC	
34	4.5708 (271.26)	0.2152	H-4→L+1 (38%) H-1→L+8 (45%)	MLCT (Ru→py) + LC (bpy)	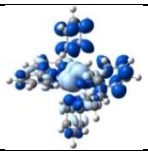
35	4.5762 (270.93)	0.0128	H-2→L+8 (18%) HOMO→L+8 (20%)	MLCT (Ru→py/bpy)	
36	4.5899 (270.12)	0.4291	H-4→L+1 (31%) H-1→L+8 (46%)	MLCT (Ru→py) + LC (bpy)	
38	4.7461 (261.24)	0.0192	HOMO→L+9 (97%)	M(L)LCT (Ru(bpy)→py)	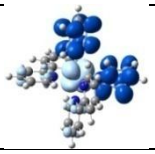

40	4.8687 (254.66)	0.0129	H-5→LUMO (14%) H-2→L+9 (79%)	MLCT (Ru→py)
45	5.2085 (238.04)	0.0274	H-3→L+2 (74%)	LC (bpy)
46	5.2255 (237.27)	0.0657	H-4→L+2 (68%)	LC (bpy)

f = oscillator strength

Table A8. TDDFT singlet-triplet transitions and corresponding electron difference density maps (EDDMs) calculated using the ^{3}MLCT geometry of *cis*-$[Ru(bpy)_2(py)_2]^{2+}$ in water at the B3LYP/LanL2DZ/6-31+G** level. In the EDDMs light blue indicates a decrease in electron density, while dark blue indicates an increase.

Tr.	E_{calc}, eV (nm)	*f*	Composition	Character	EDDMs
1	2.0146 (615.42)	0	HOMO→LUMO (89%)	M(L)LCT (Ru(bpy)→bpy)	
2	2.2471 (551.75)	0	H-1→LUMO (94%)	M(L)LCT (Ru(py)→bpy)	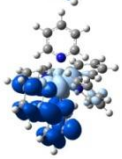
3	2.4149 (513.42)	0	H-2→LUMO (95%)	M(L)LCT (Ru(bpy/py)→bpy)	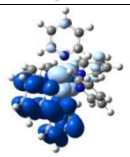
4	2.5285 (490.35)	0	HOMO→L+1 (88%)	M(L)LCT (Ru(bpy)→bpy)	

f = oscillator strength

Table A9. TDDFT singlet-triplet transitions and corresponding electron difference density maps (EDDMs) calculated using the ^{3}MLCT geometry of *cis*-$[Ru(bpy)_2(py)_2]^{2+}$ in water at the B3LYP/LanL2DZ/6-311G** level. In the EDDMs light blue indicates a decrease in electron density, while dark blue indicates an increase.

Tr.	E_{calc}, eV (nm)	*f*	Composition	Character	
1	1.9870 (623.98)	0	HOMO→LUMO (91%)	M(L)LCT (Ru(bpy)→bpy)	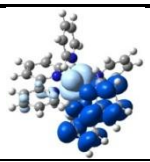

2	2.2014 (563.21)	0	H-1→LUMO (94%)	M(L)LCT (Ru(py)→bpy)	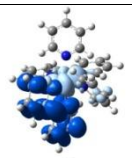
3	2.3640 (524.46)	0	H-2→LUMO (95%)	M(L)LCT (Ru(bpy/py)→bpy)	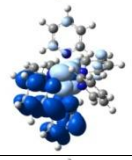
4	2.4929 (497.35)	0	HOMO→L+1 (89%)	M(L)LCT (Ru(bpy)→bpy)	

Table A10. TDDFT singlet-triplet transitions and corresponding electron difference density maps (EDDMs) calculated using the ^{3}MLCT geometry of *cis*-$[Ru(bpy)_2(py)_2]^{2+}$ in water at the PBE0/LanL2DZ/6-31+G** level. In the EDDMs light blue indicates a decrease in electron density, while dark blue indicates an increase.

Tr.	**E_{calc}**, eV (nm)	***f***	**Composition**	**Character**	**EDDMs**
1	2.0735 (597.94)	0	HOMO→LUMO (81%)	M(L)LCT (Ru(bpy)→bpy)	
2	2.3468 (528.32)	0	H-1→LUMO (86%)	M(L)LCT (Ru(py)→bpy)	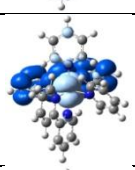
3	2.5599 (484.32)	0	H-2→LUMO (90%)	M(L)LCT (Ru(bpy/py)→bpy)	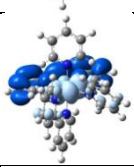
4	2.6031 (476.29)	0	HOMO→L+1 (73%)	M(L)LCT (Ru(bpy)→bpy)	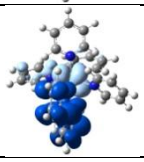

f = oscillator strength

Table A11. TDDFT singlet-triplet transitions and corresponding electron difference density maps (EDDMs) calculated using the ^{3}MLCT geometry of *cis*-$[Ru(bpy)_2(py)_2]^{2+}$ in water at the PBE0/LanL2DZ/6-311G** level. In the EDDMs light blue indicates a decrease in electron density, while dark blue indicates an increase.

Tr.	E_{calc}, eV (nm)	*f*	Composition	Character	
1	2.0578 (602.50)	0	HOMO→LUMO (83%)	M(L)LCT (Ru(bpy)→bpy)	
2	2.3125 (536.15)	0	H-1→LUMO (86%)	M(L)LCT (Ru(py)→bpy)	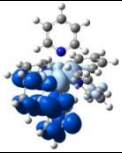
3	2.5201 (491.97)	0	H-2→LUMO (89%)	M(L)LCT (Ru(bpy/py)→bpy)	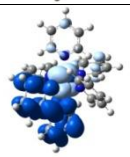
4	2.5820 (480.19)	0	HOMO→L+1 (77%)	M(L)LCT (Ru(bpy)→bpy)	

f = oscillator strength

Table A12. TDDFT singlet-triplet transitions and corresponding electron difference density maps (EDDMs) calculated using the ^{3}MC geometry (gas phase) of *cis*-$[Ru(bpy)_2(py)_2]^{2+}$ in water at the B3LYP/LanL2DZ/6-31+G** level. In the EDDMs light blue indicates a decrease in electron density, while dark blue indicates an increase.

Tr.	E_{calc}, eV (nm)	*f*	Composition	Character	EDDMs
1	0.4824 (2570.15)	0	HOMO→LUMO (68%) H-1→LUMO (20%) HOMO→L+2 (17%)	MC/MLCT (Ru→bpy)	
2	0.9011 (1375.87)	0	H-2→LUMO (35%) H-1→LUMO (35%)	MC/MLCT (Ru→bpy)	
3	0.9911 (1251.0)	0	H-2→LUMO (41%) H-1→LUMO (24%) H-2→L+2 (11%)	MC/MLCT (Ru→bpy)	
4	2.6234 (472.62)	0	HOMO→L+1 (39%) HOMO→LUMO (18%) HOMO→L+2 (-18%)	MC/MLCT (Ru→bpy)	

f = oscillator strength

Table A13. TDDFT singlet-triplet transitions and corresponding electron difference density maps (EDDMs) calculated using the ^{3}MC geometry of *cis*-$[Ru(bpy)_2(py)_2]^{2+}$ in water at the B3LYP/LanL2DZ/6-311G** level. In the EDDMs light blue indicates a decrease in electron density, while dark blue indicates an increase.

Tr.	E_{calc}, eV (nm)	*f*	Composition	Character	EDDMs
1	-0.2119 (-5851.46)	0	HOMO→LUMO (108%) HOMO→L+2 (26%) H-1→LUMO (25%)	MC/MLCT (Ru→bpy)	
2	0.6486 (1911.49)	0	H-2→LUMO (45%) H-1→LUMO (39%) H-2→L+2 (10%)	MC/MLCT (Ru→bpy)	
3	0.7973 (1555.01)	0	H-2→LUMO (42%) H-1→LUMO (32%) H-2→L+2 (10%) HOMO→LUMO (10%)	MC/MLCT (Ru→bpy)	
4	2.5522 (485.79)	0	HOMO→L+2 (69%) HOMO→LUMO (17%)	MC/MLCT (Ru→bpy)	

f = oscillator strength

Table A14. TDDFT singlet-triplet transitions and corresponding electron difference density maps (EDDMs) calculated using the ^{3}MC geometry of *cis*-$[Ru(bpy)_2(py)_2]^{2+}$ in water at the PBE0/LanL2DZ/6-31+G** level. In the EDDMs light blue indicates a decrease in electron density, while dark blue indicates an increase.

Tr.	E_{calc}, eV (nm)	*f*	Composition	Character	EDDMs
1	0.1912 (6485.73)	0	HOMO→L+2 (87%) HOMO→LUMO (78%) H-1→L+2 (13%) H-1→LUMO (12%)	MC/MLCT (Ru→bpy)	
2	0.8477 (1462.53)	0	H-2→L+2 (39%) H-2→LUMO (37%) H-1→L+2 (13%) H-1→LUMO (12%)	MC/MLCT (Ru→bpy)	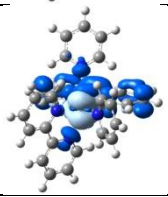
3	0.9734 (1273.68)	0	H-1→L+2 (33%) H-1→LUMO (30%) H-2→L+2 (14%) H-2→LUMO (12%)	MC/MLCT (Ru→bpy)	
4	2.6364 (470.27)	0	HOMO→LUMO (38%) HOMO→L+2 (32%)	MC/MLCT (Ru→bpy)	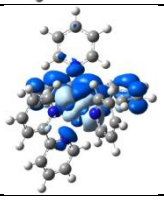

f = oscillator strength

Table A15. TDDFT singlet-triplet transitions and corresponding electron difference density maps (EDDMs) calculated using the ^{3}MC geometry of *cis*-$[Ru(bpy)_2(py)_2]^{2+}$ in water at the PBE0/LanL2DZ/6-311G** level. In the EDDMs light blue indicates a decrease in electron density, while dark blue indicates an increase.

Tr.	E_{calc}, eV (nm)	*f*	Composition	Character	EDDMs
1	-0.1589 (-7800.86)	0	HOMO→L+2 (98%) HOMO→LUMO (83%) H-1→L+2 (16%) H-1→LUMO (13%)	MC/MLCT (Ru→bpy)	
2	0.7988 (1552.05)	0	H-2→L+2 (42%) H-2→LUMO (38%) H-1→L+2 (11%) H-1→LUMO (10%)	MC/MLCT (Ru→bpy)	
3	0.928 (1335.98)	0	H-1→L+2 (35%) H-1→LUMO (31%) H-2→L+2 (12%) H-2→LUMO (10%)	MC/MLCT (Ru→bpy)	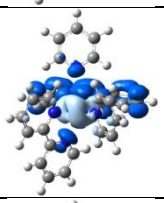
4	2.6131 (474.46)	0	HOMO→LUMO (41%) HOMO→L+2 (33%)	MC/MLCT (Ru→bpy)	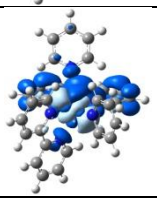

f = oscillator strength

Table A16. TDDFT triplet-triplet transitions and corresponding electron difference density maps (EDDMs) calculated using the ^{3}MLCT geometry of *cis*-$[Ru(bpy)_2(py)_2]^{2+}$ in water at the PBE0/LanL2DZ/6-311G** level. In the EDDMs light blue indicates a decrease in electron density, while dark blue indicates an increase.

Tr.	E_{calc}, eV (nm)	*f*	Composition	Character	EDDMs
10	1.6656 (744.38)	0.0232	HOMO(A)→L+7(A) (18%) HOMO(A)→L+8(A) (17%) HOMO(A)→L+9(A) (23%)	IL (bpy→py)	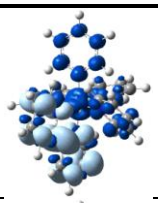
11	1.7282 (717.41)	0.0166	HOMO(A)→L+4(A) (11%) HOMO(A)→L+9(A) (56%)	LC/IL (bpy→py)	

f = oscillator strength

Table A17. TDDFT triplet-triplet transitions and corresponding electron difference density maps (EDDMs) calculated using the ^{3}MC geometry of *cis*-$[Ru(bpy)_2(py)_2]^{2+}$ in water at the PBE0/LanL2DZ/6-311G** level. In the EDDMs light blue indicates a decrease in electron density, while dark blue indicates an increase.

Tr.	E_{calc}, eV (nm)	*f*	Composition	Character	EDDMs
3	1.9634 (631.47)	0.0060	HOMO(B)→L+3(B) (12%) HOMO(B)→L+6(B) (24%) HOMO(B)→L+9(B) (19%)	MC/MLCT (Ru→py/bpy)	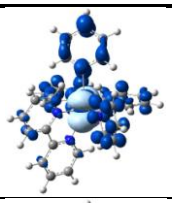
2	2.1356 (580.56)	0.0044	HOMO(A)→LUMO(A) (87%) HOMO(B)→L+1(B) (3%) HOMO(B)→L+6(B) (2%)	M(L)LCT (Ru(bpy/py)→bpy)	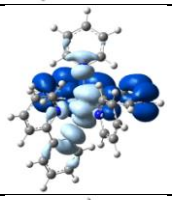
5	2.7850 (445.17)	00290	H-1(B)→L+1(B) (19%) H-1(B)→L+3(B) (13%) H-1(B)→L+6(B) (22%) H-1(B)→L+9(B) (17%)	MLCT (Ru→bpy)	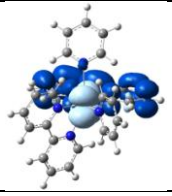

f = oscillator strength

A4. Spin density surfaces

Table A18. Spin density surfaces and SOMO orbitals for the ^{3}MLCT geometry of *cis*-$[Ru(bpy)_2(py)_2]^{2+}$ calculated in water with the B3LYP and PBE0 functional.

	Spin density		l-SOMO	h-SOMO
B3LYP LanL2DZ/6-31+G**	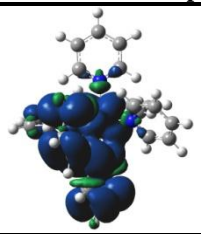	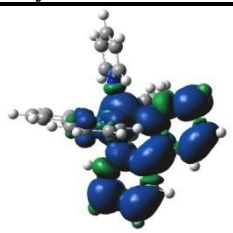	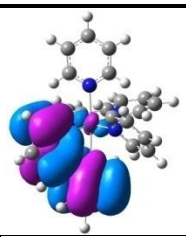	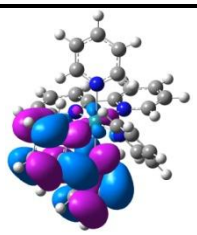
B3LYP LanL2DZ/6-311G**	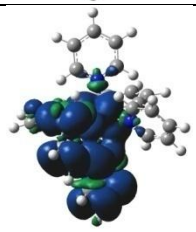	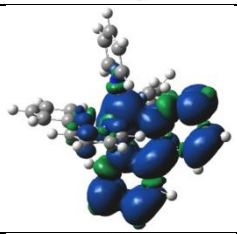	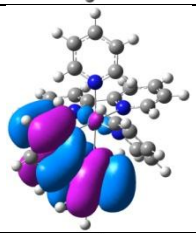	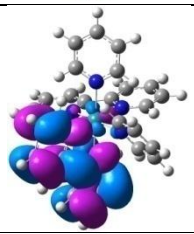
PBE0 LanL2DZ/6-31+G**	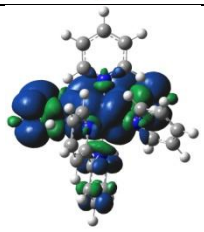	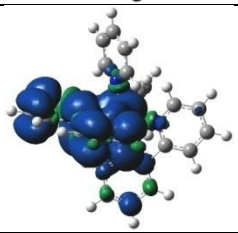	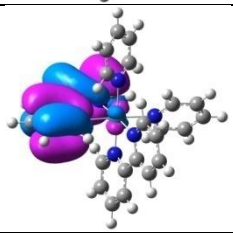	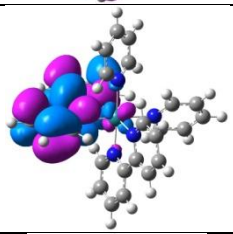
PBE0 LanL2DZ/6-311G**	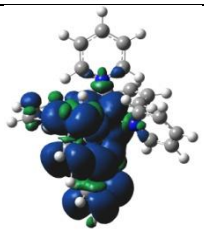	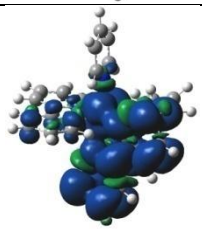	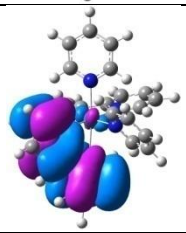	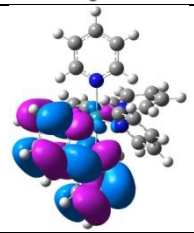

Table A19. Spin density surfaces and SOMO orbitals for the ^{3}MC geometry of *cis*-$[Ru(bpy)_2(py)_2]^{2+}$ calculated in water with the B3LYP and PBE0 functional.

	Spin density		l-SOMO	h-SOMO
B3LYP LanL2DZ/6-31+G** *Gas phase*	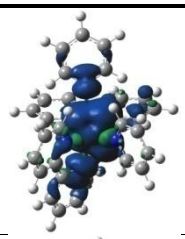	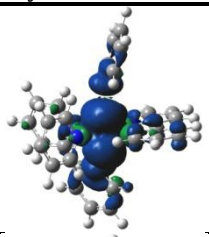	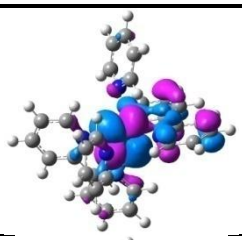	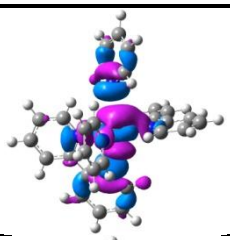
B3LYP LanL2DZ/6-311G**	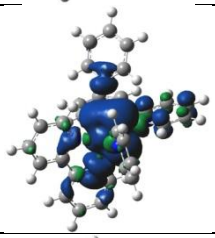	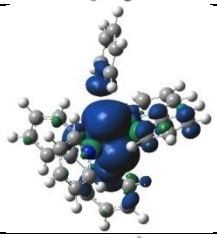	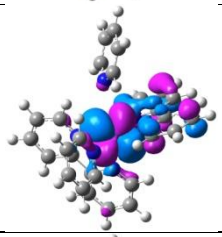	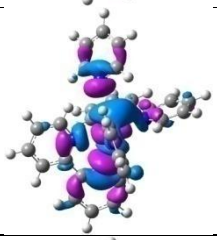
PBE0 LanL2DZ/6-31+G**	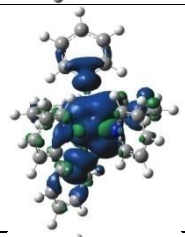		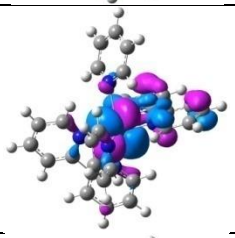	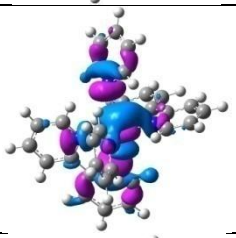
PBE0 LanL2DZ/6-311G**	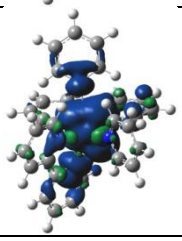	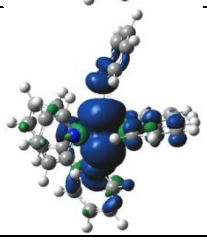	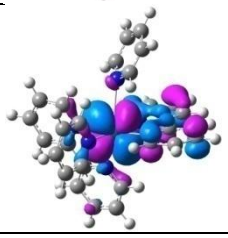	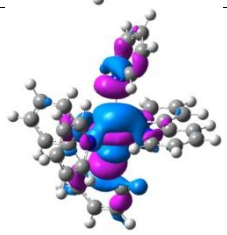

A5. Triplet excited state energies

Table A20. Emission energy for the ^{3}MLCT state of *cis*-$[Ru(bpy)_2(py)_2]^{2+}$calculated with the ΔSCF method in water.

	ΔSCF (eV)	ΔSCF (nm)
B3LYP LanL2DZ/6-31+G**	2.053	604
B3LYP LanL2DZ/6-311G**	1.997	621
PBE0 LanL2DZ/6-31+G**	2.031	610
PBE0 LanL2DZ/6-311G**	1.980	626

Table A21. Energy difference for the ^{3}MLCT and ^{3}MC states of *cis*-$[Ru(bpy)_2(py)_2]^{2+}$ in water.

	ΔE (^{3}MLCT–^{3}MC) (eV)
B3LYP LanL2DZ/6-31+G**	n.d.
B3LYP LanL2DZ/6−311G**	0.458
PBE0 LanL2DZ/6-31+G**	0.309
PBE0 LanL2DZ/6-311G**	0.278
TPSSh LanL2DZ/6-311G**	0.144
M06 LanL2DZ/6-311G**	0.624
mPW1PBE LanL2DZ/6-311G**	0.294
mPW1LYP LanL2DZ/6-311G**	0.540
m062X LanL2DZ/6-311G**	0.919
HSEh1PBE LanL2DZ/6-311G**	0.281
Average	**0.427**
Standard Deviation	**0.237**

n.d.= not determined. All our attempts to optimize the ^{3}MC geometry at the B3LYP/6-31+G** with the CPCM solvent model were not successful.

Table A22. Energy difference for the ^{3}MLCT and ^{3}MC states of *cis*-$[Ru(bpy)_2(py)_2]^{2+}$in dichloromethane.

	ΔE (^{3}MLCT–^{3}MC) (eV)
PBE0 LanL2DZ/6-311G**	0.294
TPSSh LanL2DZ/6-311G**	0.156
M06 LanL2DZ/6-311G**	0.638
m062X LanL2DZ/6-311G**	0.929
Average	**0.504**
Standard Deviation	**0.348**

A6. ECP dependence

Table A23. Calculated bond lengths for the singlet ground state (GS) and triplet ^{3}MLCT and ^{3}MC states of *cis*-$[Ru(bpy)_2(py)_2]^{2+}$ in water at the PBE0/6-311G** level. Solvent effects were included using the CPCM method. The LanL2TZ, LanL08 and SDD ECP were employed for the Ru atom.

Bond lengths – GS						
	Ru–N1(bpy)	**Ru–N2(bpy)**	**Ru–N13(bpy)**	**Ru–N14(bpy)**	**Ru–N42(py)**	**Ru–N53(py)**
PBE0/ SDD/6-311G**	2.06507	2.08024	2.06507	2.08024	2.12268	2.12268
PBE0/ LANL2TZ/6-311G**	2.07792	2.09338	2.07792	2.09338	2.13546	2.13546
PBE0/ LANL08/6-311G**	2.07793	2.09339	2.07792	2.09339	2.13546	2.13546
Bond lengths – ^{3}MLCT						
	Ru–N1(bpy)	**Ru–N2(bpy)**	**Ru–N13(bpy)**	**Ru–N14(bpy)**	**Ru–N42(py)**	**Ru–N53(py)**
PBE0/ SDD/6-311G**	2.02431	2.05460	2.06123	2.10166	2.12835	2.15409
PBE0/ LANL2TZ/6-311G**	2.03277	2.06379	2.07188	2.11492	2.13970	2.16717
PBE0/ LANL08/6-311G**	2.03278	2.06379	2.07189	2.11492	2.13970	2.16717
Bond lengths – ^{3}MC						
	Ru–N1(bpy)	**Ru–N2(bpy)**	**Ru–N13(bpy)**	**Ru–N14(bpy)**	**Ru–N42(py)**	**Ru–N53(py)**
PBE0/ SDD/6-311G**	2.34561	2.14324	2.08619	2.07933	2.12780	2.81406
PBE0/ LANL2TZ/6-311G**	2.36307	2.16182	2.09947	2.09402	2.14031	2.80064
PBE0/ LANL08/6-311G**	2.36311	2.16183	2.09950	2.09403	2.14029	2.80034

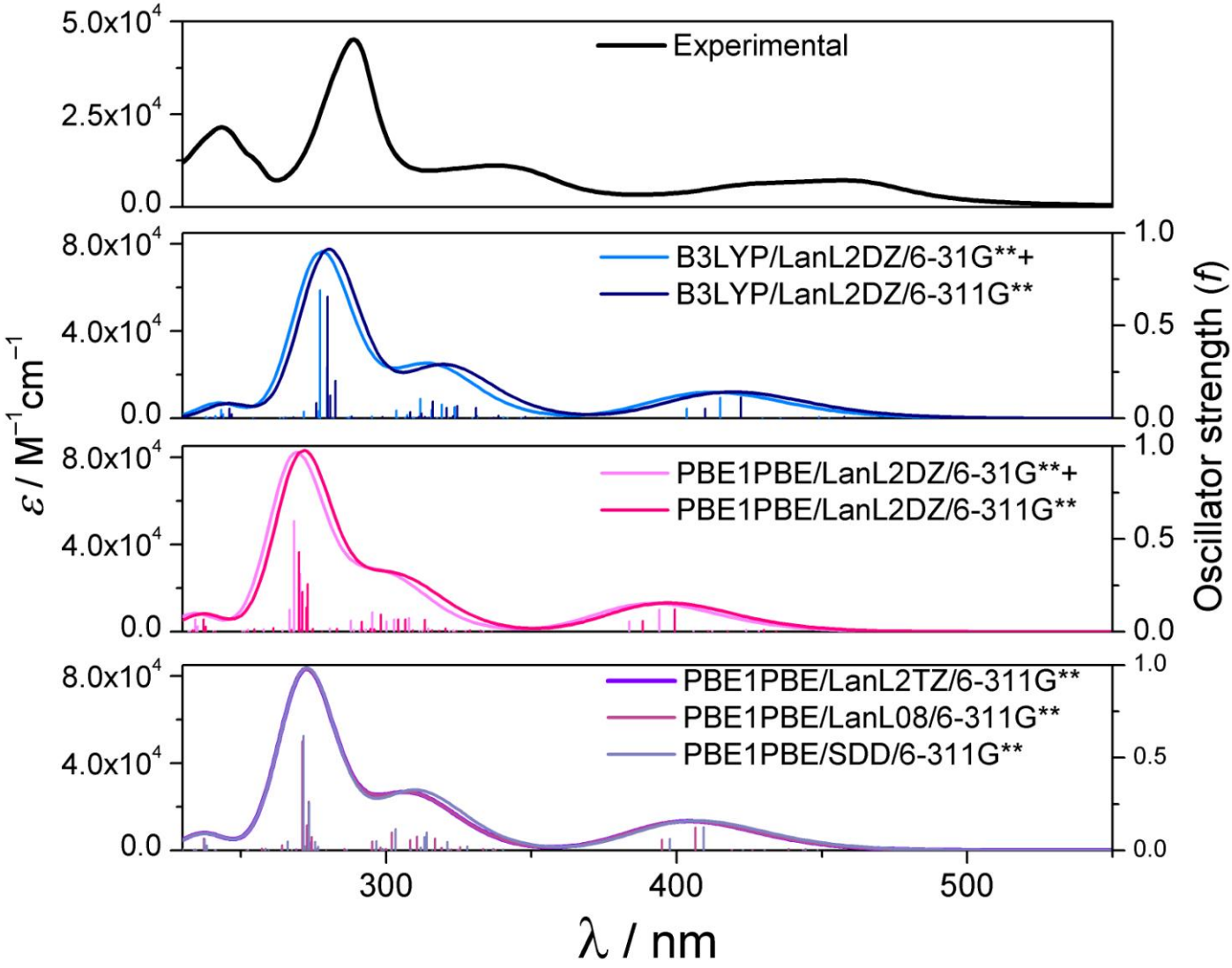

Figure A2. Experimental (black line) and calculated (colored lines) absorption spectra of *cis*-$[Ru(bpy)_2(py)_2]^{2+}$ in water. The singlet excited transitions are shown as vertical bars with heights equal to the extinction coefficients. The theoretical curve was obtained using the program GAUSSSUM 1.05.

Table A24. Spin density surfaces and SOMO orbitals for the ^{3}MLCT geometry of *cis*-$[Ru(bpy)_2(py)_2]^{2+}$ calculated in water at the PBE0/6-311G** level using the LanL2TZ, LanL08 and SDD ECP for the Ru atom.

	Spin density		l-SOMO	h-SOMO
PBE0/ SDD/6-311G**	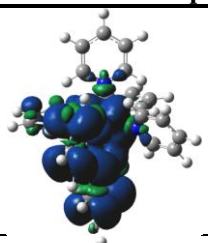	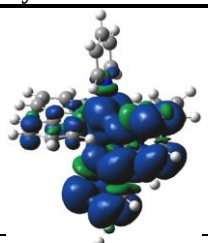		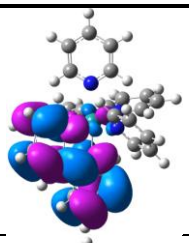
PBE0/ LANL2TZ/6-311G**	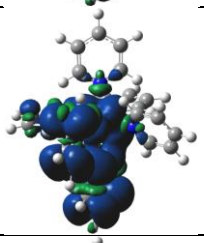	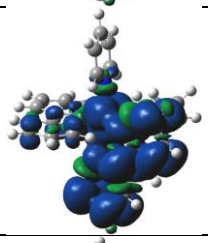	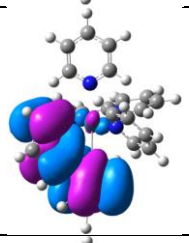	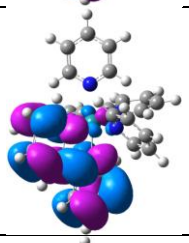
PBE0/ LANL08/6-311G**	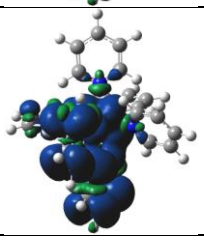	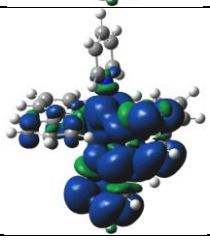	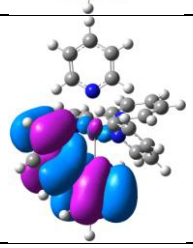	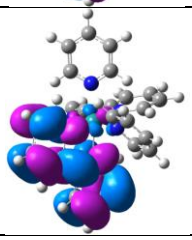

Table A25. Spin density surfaces and SOMO orbitals for the ^{3}MC geometry of *cis*-$[Ru(bpy)_2(py)_2]^{2+}$ calculated in water at the PBE0/6-311G** level using the LanL2TZ, LanL08 and SDD ECP for the Ru atom.

	Spin density		l-SOMO	h-SOMO
PBE0/ SDD/6-311G**	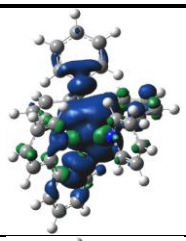	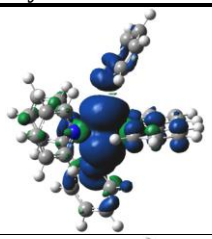	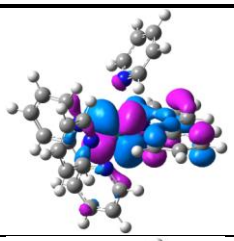	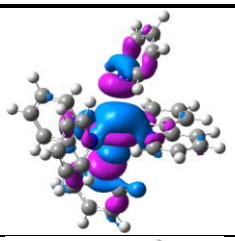
PBE0/ LANL2TZ/6-311G**	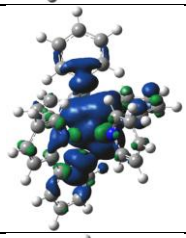	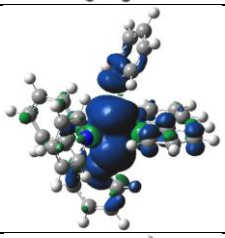	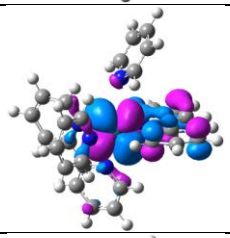	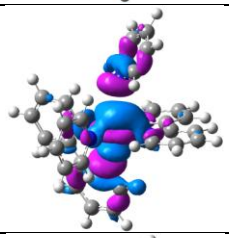
PBE0/ LANL08/6-311G**	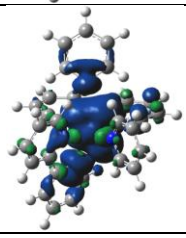	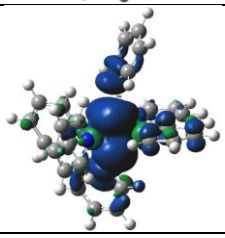	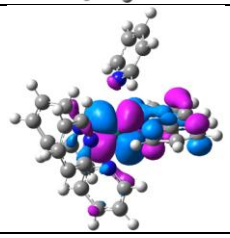	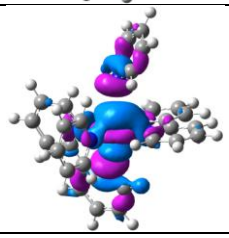

B – Optical Transient Absorption (OTA)

B1. Transient absorption results

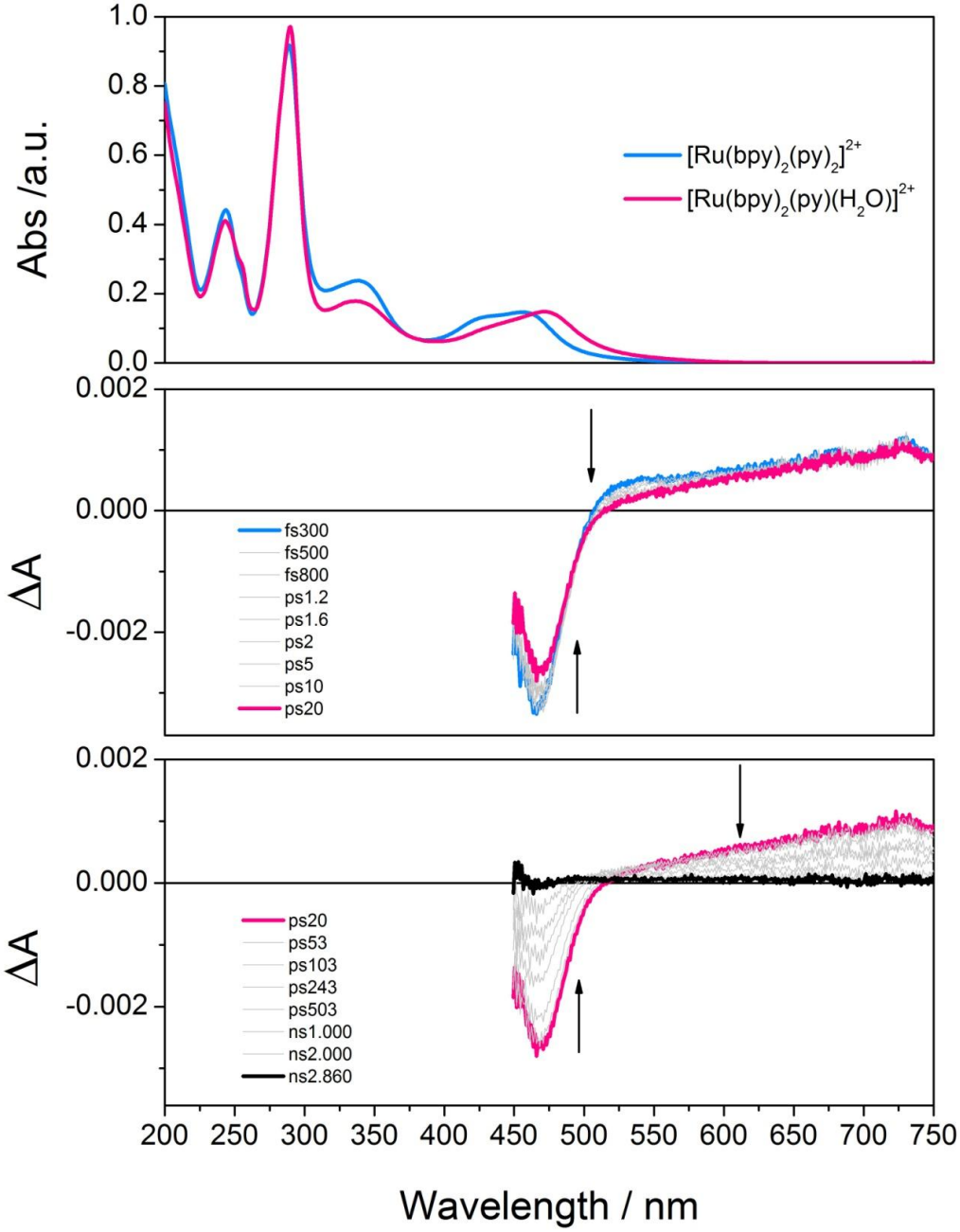

Figure B1. ***Top:*** UV-Vis absorption spectrum of *cis*-$[Ru(bpy)_2(py)_2]^{2+}$ (light blue) and *cis*-$[Ru(bpy)_2(py)(H_2O)]^{2+}$ + py (pink) in aqueous solution. The latter was obtained by photolysis of *cis*-$[Ru(bpy)_2(py)_2]^{2+}$ with 420 nm light (λ_{exc} = 420 nm, 20 mW/cm^2, 10 min). ***Middle:*** OTA spectra of aqueous *cis*-$[Ru(bpy)_2(py)_2]^{2+}$ in the range 300 fs − 20 ps. ***Bottom:*** OTA spectra of aqueous *cis*-$[Ru(bpy)_2(py)_2]^{2+}$ in the range 20 ps − 2.86 ns.

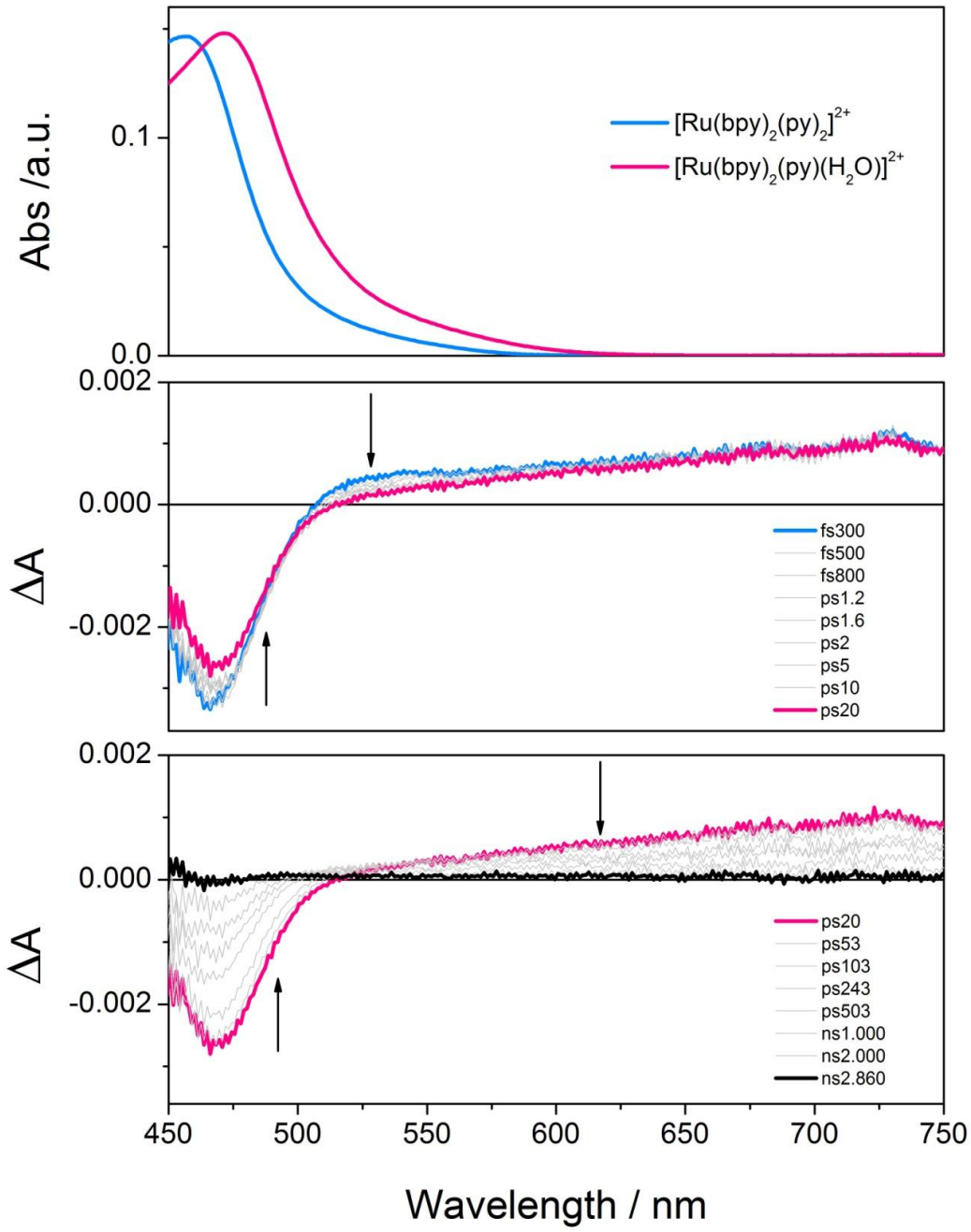

Figure B2. ***Top:*** Zoom in the UV-Vis absorption spectrum of *cis*-$[Ru(bpy)_2(py)_2]^{2+}$ (light blue) and *cis*-$[Ru(bpy)_2(py)(H_2O)]^{2+}$ + py (pink) in aqueous solution. The latter was obtained by photolysis of *cis*-$[Ru(bpy)_2(py)_2]^{2+}$ with 420 nm light (λ_{exc} = 420 nm, 20 mW/cm^2, 10 min). ***Middle:*** Zoom in the OTA spectra of aqueous *cis*-$[Ru(bpy)_2(py)_2]^{2+}$ in the range 300 fs − 20 ps. ***Bottom:*** Zoom in the OTA spectra of aqueous *cis*-$[Ru(bpy)_2(py)_2]^{2+}$ in the range 20 ps − 2.86 ns.

Table B1. Decay fitting parameters in the 467–723 nm range.

	467 nm	**484 nm**	**651 nm**	**700 nm**	**723 nm**
A1	-0.00137 ±0.00006	-0.00125 ±0.00004	0.00025 ±0.00003	0.00028 ±0.00003	0.0003 ±0.00003
τ_1(ps)	130±7	130±7	130±7	130±7	130±7
A2	-0.00187 ±0.00009	-0.00094 ±0.00006	0.00056 ±0.00005	0.00073 ±0.00006	0.00087 ±0.00006
τ_2(ps)	1700±200	1700±200	1700±200	1700±200	1700±200
A0	0.0002±0.0001	0.00037±0.00007	-0.00002±0.00005	-0.00005±0.00006	-0.00010±0.00007

Table B2. Decay fitting parameters in the 500–550 nm range.

	502 nm	**517 nm**	**527 nm**	**540 nm**
A3	0.00026 ±0.00001	0.00034 ±0.00001	0.00032 ±0.00001	0.00031 ±0.00001
τ_3(ps)	1.30±0.03	1.30±0.03	1.30±0.03	1.30±0.03
A0	-0.000360 ±5E-6	0.000060 ±8E-6	0.000170 ±5E-6	0.000220 ±5E-6

C – XTA

C1. XTA experimental setup

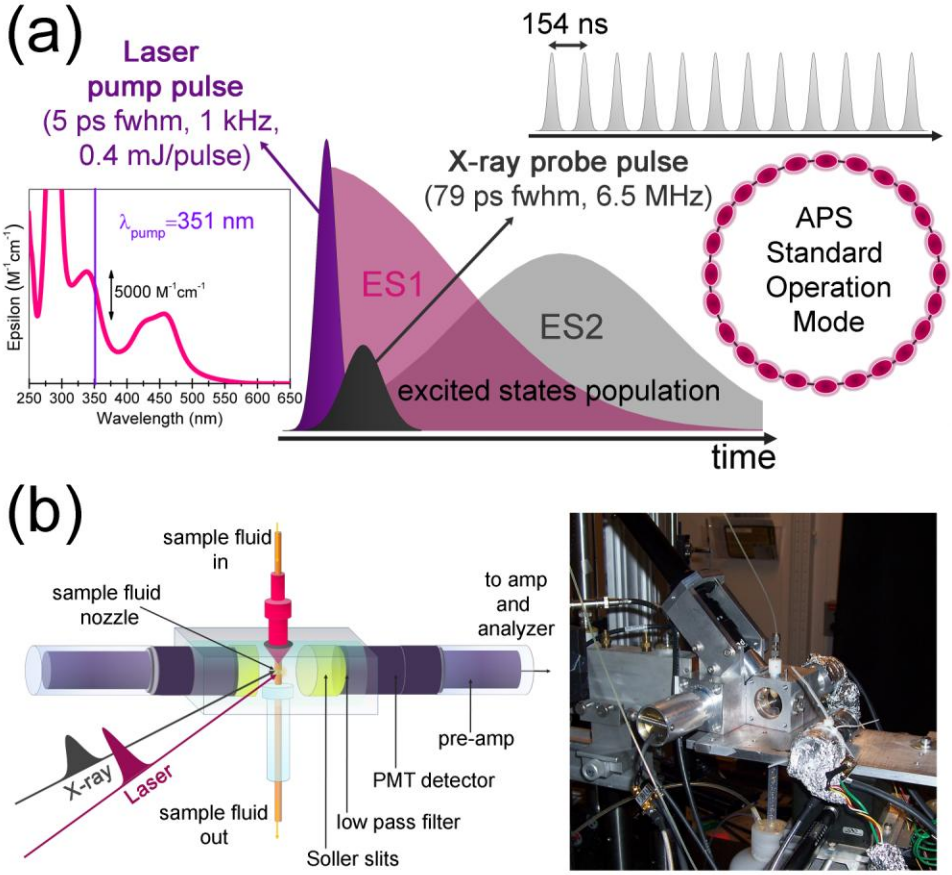

Figure C1. Experimental setup for XTA measurements at the APS 11ID-D beamline. (a) Pump/probe pulses features. (b) Detailed scheme (left panel) and photograph (right panel) of the sample cell, specifically designed for measurements on dilute solutions.

C2. XTA data acquisition and reduction strategy

For each selected time delay τ (τ = 150 ps, 500 ps and 3000 ps) a series of 40 scans, each including (i) an ES spectrum from the fluoresce signals of the synchronized X-ray pulse at certain delay after the laser pump pulse excitation; (ii) a GS spectrum from fluorescence signals of the same X-ray pulse averaged over its 50 round trips in the storage ring prior to the laser pulse and (iii) a reference ruthenium metal foil spectrum for energy alignment, was collected. The solution (500 mL 1 mM) was replaced after ca. 3 h of laser irradiation, to avoid undesired photoproduct accumulation in the probed volume. Pre-edge region and XANES part of the spectra were acquired with a constant energy step of 5, 2 and 1 eV in the regions E_{edge}−150 eV < E < E_{edge}−30 eV, E_{edge}−30 eV < E < E_{edge}−15 eV, and E_{edge}−15 eV< E < E_{edge}+20 eV, respectively. The EXAFS part (from k = 2 $Å^{-1}$up to 12 $Å^{-1}$) was collected using a constant Δk = 0.05 $Å^{-1}$, resulting in a variable sampling step in energy. The

integration time per point was of 4 s for the pre-edge and XANES regions and linearly variable from 5 to 30 s in the EXAFS part of the spectrum. The extraction of the $\chi(k)$ functions was performed using the Athena programs.[20] After extraction, ES and GS spectrum for each scan were aligned using the reference metal foil, obtaining an array of $[\chi_i^{GS}(k), \chi_i^{ES}(k,\tau)]$ curves, for $1 < i < 40$ (number of scan). The difference spectra $\Delta\chi_i(k, \tau) = \chi_i^{ES}(k, \tau) - \chi_i^{GS}(k)$ were then computed for each scan, and then averaged on the 40 scans of a series, in k-space. The $\chi_i^{GS}(k)$ spectra acquired for all the scans and for each time delay were globally averaged to obtain an high-statistics GS spectrum, namely $\chi^{GS}(k)$, to be used as starting point for the differential analysis procedure (see Section C4).

The average $\Delta\chi(k, \tau)$ transient spectra are reported in Figure C2 for τ = 150, 500 and 3000 ps (green, blue and pink circles, respectively). It is evident that, also if averaged on a number of acquisitions noticeably higher that that routinely used in EXAFS static experiments, the curves are characterized by a quite low signal-to-noise ratio. Notwithstanding the noisy appearance, the curves for the three selected delays differ significantly one from each other, especially in the intensity of the first differential oscillation and in the position of the minimum at ca. 2.7 $Å^{-1}$. A Fourier filtering procedure was then applied to raw $\Delta\chi(k, \tau)$ curves: the EXAFS signal was first Fourier transformed from k- to R-space using the k range 2.5 $Å^{-1}$ – 10.8 $Å^{-1}$, and then was back-Fourier transformed into momentum space only in the R-range 1.0 Å – 5.0 Å (where the physical signal is expected). After the filtering operation, the momentum space will be named as q-space to be distinguished from the starting k-space. Filtered $\Delta\chi(q, \tau)$ and raw $\Delta\chi(k, \tau)$ differential spectra are separately compared for each time delay in Figure C2.

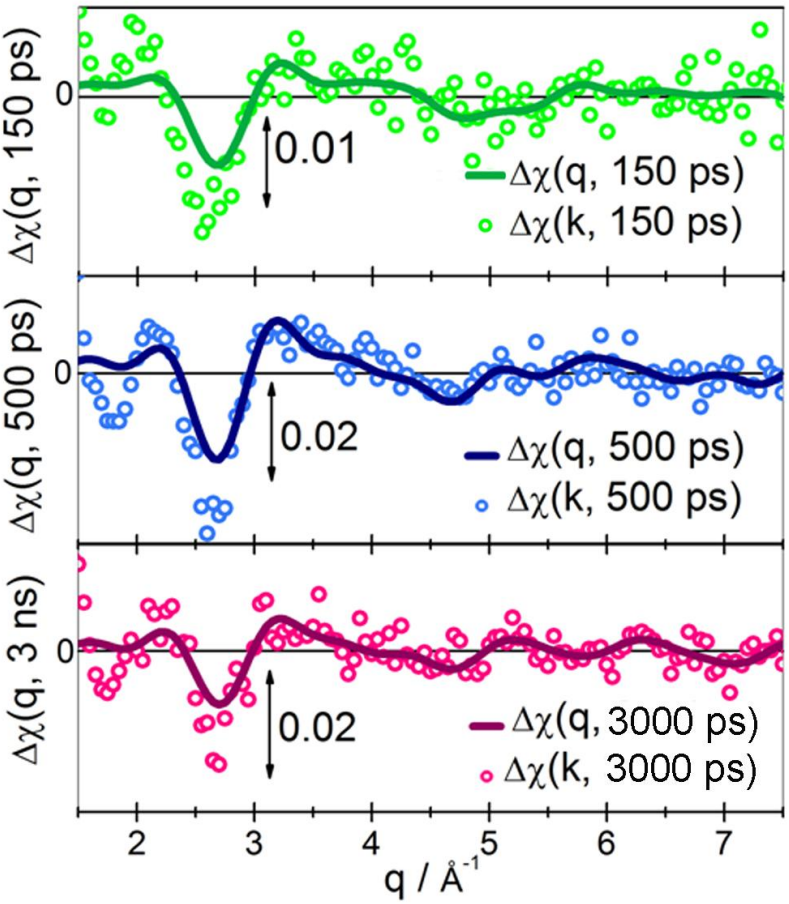

Figure C2. $\Delta\chi(k, \tau)$ transient spectra for τ = 150, 500 and 3000 ps (green, blue and magenta circles, respectively) calculated as the average on all the scans of the differences $\Delta\chi_i(k, \tau) = \chi_i^{ES}(k, \tau) - \chi_i^{GS}(k, \tau)$ obtained for each scan, in k-space. $\Delta\chi(k, \tau)$ differential spectra for each delay are compared with respective Fourier filtered $\Delta\chi(q, \tau)$ curves (k range 2.5 − 10.8 $Å^{-1}$ for the forward FT, R-range 1.0 − 5.0 Å for the backward FT), shown as dark green, dark blue and purple solid lines, respectively.

C3. Details on differential method for EXAFS structural refinement and its application to *cis*-$[Ru(bpy)_2(py)_2]^{2+}$ photoreaction

It has recently been shown that the precision in determining structural parameters using XTA can be further enhanced by a quantitative structural analysis of the excited state.[21] This approach is based on the fitting of the differential transient EXAFS spectrum directly in energy/momentum space by minimization of the square residual function between a large series of simulated differential EXAFS spectra and the experimental transient data. This method provides a superior accuracy for the derived structural parameters if compared to conventional EXAFS fitting methods, where structural modifications are extracted from the Fourier transform of the reconstructed excited-state EXAFS signal.[21] EXAFS signals $\chi_i^{ES}{}_{fit}(\{P\}_i, k)$ for a series of candidate excited state geometries, characterized by a set of parameters $\{P\}_i$ (bond lengths, Debye Waller parameters σ^2, edge energy shift ΔE), are generated by using the FEFF6 code included in the IFEFFIT software package.[20] The simulated

signals are converted into q-space, using the same k and R ranges adopted for the Fourier filtering of experimental data (see Section C2). Subsequently, the best fit curve $\chi^{GS}_{fit}(q)$ obtained from a standard EXAFS analysis of the GS EXAFS signal (see Section C4) is subtracted to each simulated $\chi_i^{ES}{}_{fit}(\{P\}_i, q)$ spectrum. The resulting simulated differential spectra $\Delta\chi_i^{ES}{}_{fit}(\{P\}_i, q)$ are compared with the experimental differential signal $\Delta\chi^{ES}_{exp}$ using the R-factor parameter defined by eq. (S1), where the index j runs from 1 to the total number of experimental points.

$$R_i = \sqrt{\frac{\sum_j (\Delta\chi^{ES}_{exp,j} - \Delta\chi^{ES}_{fit,j})^2}{\sum_j (\Delta\chi^{ES}_{exp,j})^2}} \qquad \text{(S1)}$$

The procedure for EXAFS differential refinement is summarized in the following Scheme C1.

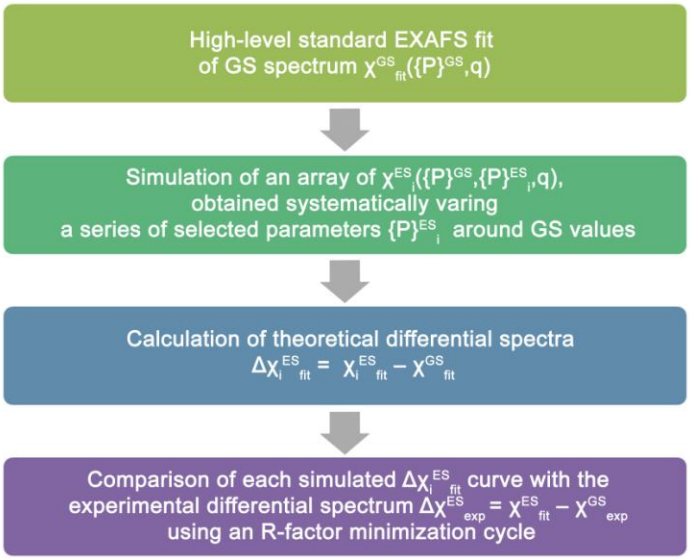

Scheme C1. Flow-chart for EXAFS data differential refinement.

The photoreaction model proposed for *cis*-$[Ru(bpy)_2(py)_2]^{2+}$ involves two excited states (^{3}MLCT and ^{3}MC), each characterized by a specific set of structural distortions with respect to the GS geometry. In addition, a third set of independent parameters is required for the stable aquo photoproduct *cis*-$[Ru(bpy)_2(py)(H_2O)]^{2+}$ (PHP). The structure of PHP is very similar to the GS one, at least from an EXAFS perspective. In fact, with the exception of some small distortion in the bond lengths, the first shell signal is expected to be only minimally perturbed after the substitution of the nitrogen of the dissociated py ring with the almost iso-electronic oxygen of the water molecule. The higher shells suffer of the signal loss due to lacking scattering paths related to a py ring, however the cumulative contribution of such paths can be estimated to be only 1/6 of the global signal (loss of 1 over 6 rings, 2 py rings and 4 rings associated in 2 bpy units).

A "one-shot" complete fitting model, simultaneously including all the possible intermediate structures, is not feasible (at least in the limit of available data quality) due to (i) the extremely high number of parameters needed, (ii) their not-negligible cross-correlations, (iii) the huge amount of machine and

human time required to generate via FEFF all the $\chi^{ES}_j(\{P\}_j, q)$ spectra that such global model would require. The approach proposed here relies on a "step by step" strategy, based on the combination of optical (OTA) and structural X-ray based ultrafast techniques (XTA) with DFT calculations.
The main steps of data analysis are summarized in Scheme C2. First of all, an extremely accurate fit of the GS spectrum, namely $\chi^{GS}_{fit}(q)$ is obtained (more details in Section C4). The $\chi^{GS}_{fit}(q)$ spectrum is used in the calculation of the $\Delta\chi_i^{ES}{}_{fit}(\{P\}_i, q) = \chi_i^{ES}{}_{fit}(\{P\}_i, q) - \chi^{GS}_{fit}(q)$ simulated differences. Moreover, the parameters values obtained from the standard EXAFS fitting procedure provide the central nodes of the variation grid along each dimension in the *N*-dimensional space corresponding to *N* simultaneously varied parameters. The following step consists in the analysis of the static EXAFS spectrum of the PHP (see Section C5), using the differential method described above. This preliminary analysis is fundamental to obtain structural parameters for the PHP that can be employed in the analysis of the XTA data. Briefly, the two main reasons for adopting a differential approach are:

(i) it is very difficult to discriminate two very similar structures as GS and PHP using an EXAFS standard approach. On the contrary, the use of a differential approach can provide an experimentally optimized structure for PHP, suitable for the subsequent interpretation of transient data;

(ii) The application of the differential method to a static problem can be regarded as a feasibility test on a set of data characterized by a good signal-to-noise ratio, before starting the same kind of refinement on the more complex time-resolved dataset.

OTA measurements highlight the presence of two time components (τ_{long} = 1700 ps and τ_{short} = 130 ps). The longer component can be safely assigned to the ^{3}MLCT ES lifetime. Conversely, the interpretation of the shorter contribution is more controversial, however it can be tentatively related to the ^{3}MC/photochemistry pathway. Although OTA data alone are not informative on the photoinduced structural distortions of the complex, the synergic combination of OTA results and DFT calculation is useful to orient the fitting procedure of XTA data (see section C6). Moreover, XTA analysis provides in turn a feedback control on the longer OTA time-component assignment and elucidates the structural distortions in the ^{3}MLCT state.

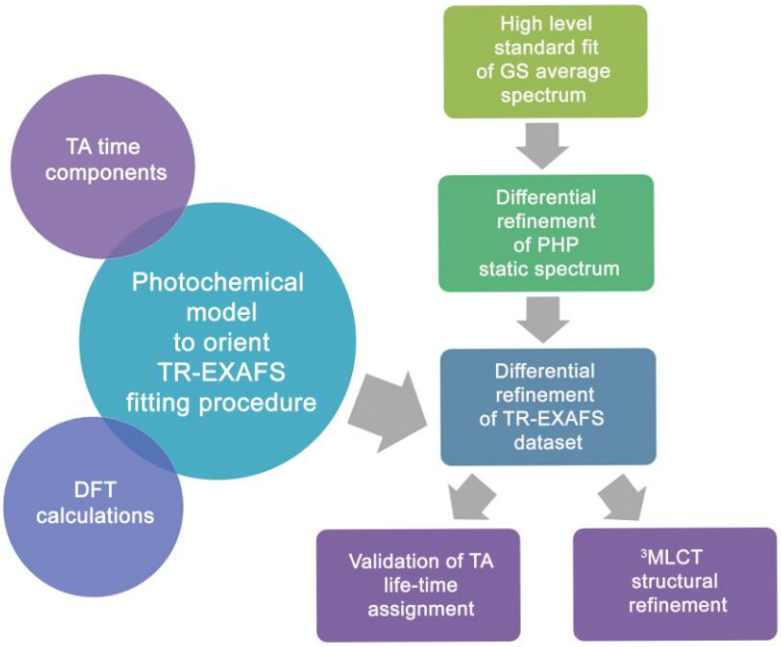

Scheme C2. Schematic representation of the main steps of data analysis, based on the combination of OTA results with DFT calculations to orient the fitting procedure of XTA dataset.

C4. Details on GS spectrum EXAFS fit and comparison between static spectra of GS and aquo-photoproduct

An high-statistic GS spectrum $\chi^{GS}_{exp}(k)$ was obtained averaging the $\chi_i^{GS}(k)$ spectra acquired for all scans and all time delays. This average GS spectrum was FT filtered choosing for the backward and forward FT the same k and R ranges used to smooth the transient data (2.5 − 10.8 $Å^{-1}$; 1.0 − 5.0 Å). Several trials were performed, systematically selecting the fitting space among k-, q- and R-space, and tuning the starting parameter values to get the best configuration in terms of fit goodness in q-space (where the XTA dataset has been analyzed) and physical meaningfulness of the parameters. The best results were obtained fitting in R-space, in the range $\Delta R = 1.0 – 5.0$ Å ($2\Delta k \Delta R/\pi \sim 21$), the k-weighted FT function, in the 2.5 – 10.8 $Å^{-1}$ k-range. The k-weighted FT functions for the experimental (black circles) and best fit spectra (gray solid lines) are reported in Figure C3a, for both the imaginary part (top panel) and the modulus (bottom panel). Phase and amplitude functions of each path were calculated by the FEFF code[20] using the DFT optimized GS structure (PBE0/LanL2DZ/6-311G**) as input. All the EXAFS paths up to R = 5.0 Å have been included in the fitting model. To limit the number of optimized variables, all paths were optimized with the same amplitude factor (S_0^2) and with the same energy shift (ΔE) parameter. Moreover, both the pairs of py and bpy ligands were considered as rigid objects, whose only degree of freedom was the radial translation along the corresponding Ru–N axis. Consequently, the only two structural parameters optimized in the fit were the distances $R_{Ru–N(py)}$ and $R_{Ru–N(bpy)}$; the lengths of all the other paths were calculated starting from these two values, according to geometrical constraints imposed by the rigidity of the py and bpy rings. Concerning the

Debye-Waller (DW) factors, only two parameters were optimized: $\sigma^2_{N(py)}$ and $\sigma^2_{N(bpy)}$, associated to Ru–N bonds for py or bpy ligands, respectively. For single scattering (SS) and multiple scattering (MS) paths involving n atoms of the same ligand, we imposed the corresponding DW factor to be $\sigma^2 = n\sigma^2_{N(L)}$ (L = py or bpy). Several almost co-linear MS paths involve two N atoms of two opposite L and L' ligands. In these cases DW factors were calculated as $\sigma^2_{MS} = \sigma_{N(L)}{}^2 + \sigma_{N(L')}{}^2$. In summary, the fit runs over 6 independent parameters.

To demonstrate how the use of a differential approach is advantageous already in the static case analysis, we compared in Figure C3 the EXAFS spectra of the GS complex and of its aquo-photoproduct (PHP). The striking similarity between the two spectra can be noticed in the figure, where the normalized μx(E) spectra for the GS (obtained as the average of all the laser-off acquisitions within the XTA dataset) and for the PHP (collected on the EXAFS beamline BM26 at the ESRF) are reported.[22] The two experimental spectra plotted in q-space are compared in Figure C3c; spectrum $\chi^{GS}_{exp}(q)$ for the GS and spectrum $\chi^{PHP}_{exp}(q)$ for the PHP.

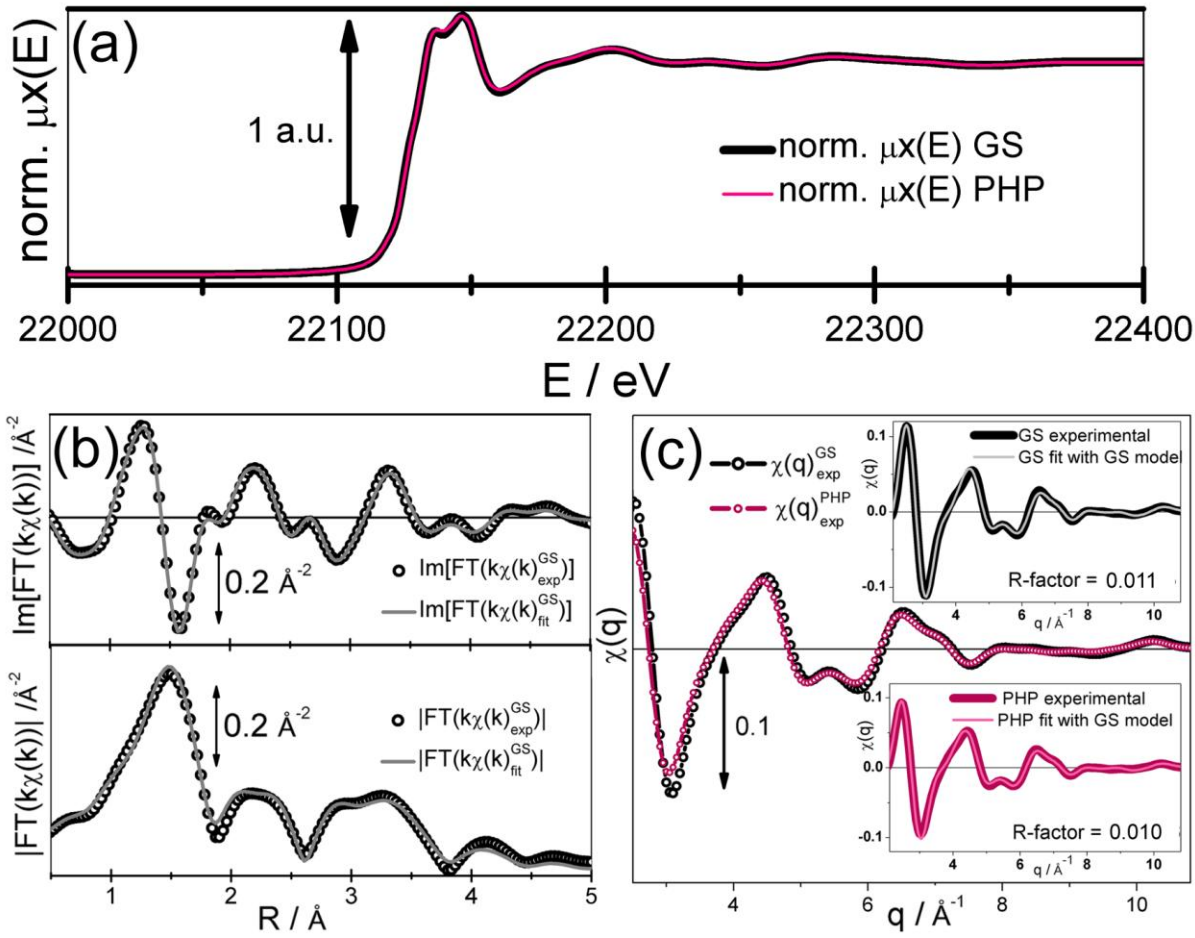

Figure C3. (a) Normalized μx(E) spectra for GS (black solid line), obtained as the average of all the laser-off acquisitions within the XTA dataset, and for PHP (magenta solid line), collected on the EXAFS beamline BM26 at the ESRF. (b) Fitting of GS spectrum $\chi^{GS}_{exp}(q)$: k-weighted FT functions for the experimental (black circles) and best fit curves (gray solid lines) are reported both for the imaginary part (top panel) and the

modulus (bottom panel). (c) Comparison between $\chi^{GS}_{exp}(q)$ for GS and $\chi^{PHP}_{exp}(q)$ for PHP. In the upper inset: best fit $\chi^{GS}_{exp}(q)$ (gray thin line) compared with $\chi^{GS}_{exp}(q)$ experimental spectrum (black thick line); in the bottom inset: test fit on the $\chi^{PHP}_{exp}(q)$ spectrum, using exactly the same conditions adopted in the case of the $\chi^{GS}_{exp}(q)$ spectrum fit, in terms of selected fitting-space, number and features of included paths and parameters starting values.

To confirm the inadequacy of a standard EXAFS fitting procedure in discriminating among the GS and PHP structures, a test fit was performed on the $\chi^{PHP}_{exp}(q)$ spectrum, using exactly the same conditions adopted for the $\chi^{GS}_{exp}(q)$ spectrum fitting, in terms of selected fitting-space, number and parametrization of included paths and starting values (see Insets of Figure C3c). In this case the coordination number for the N(py) atoms imposed in the fit (N_{py}^{fit}) is thus equal to two, and differs from the effective coordination number $N_{py}^{eff} = 1$, being one py unit substituted by the H_2O molecule. This fit is characterized by an R-factor value of ~ 1%, as in the case of the $\chi^{GS}_{exp}(q)$ best fit, and by refined parameters values perfectly comparable with the ones found for the $\chi^{GS}_{exp}(q)$ curve, within their experimental error. The effective missing of a py unit in the PHP structure is well compensated by a slight increase of the associated DW factor σ^2_{py}, from (0.0032 ± 0.0008) Å^2 to (0.0041 ± 0.0009) Å^2. The results are reported in Table C1, and are fully compatible with what obtained from previous EXAFS static studies on the same and on very similar complexes.[23-25]

Table C1. Results from EXAFS analysis of GS and PHP spectra $\chi^{GS}_{exp}(k)$ and $\chi^{PHP}_{exp}(k)$. The fits were performed in R-space in the $\Delta R = 1.00 - 5.00$ Å range, over k-weighted FT of the $\chi(k)$ functions in the $2.5 - 10.8$ Å^{-1} range. A single ΔE_0 and a single S_0^2 have been optimized for all SS and MS paths. Coordination numbers for N(L) atoms, where L = py or bpy, are reported, distinguishing between values imposed in the fit (N_L^{fit}) and effective values (N_L^{eff}). The same structural model of the GS complex was employed in the photoproduct test fit, thus in this case $N_{py}^{fit} = 2 \neq N_{py}^{eff} = 1$. Both fits are characterized by a very good R-factor value, ~ 1%, and give parameters values almost identical in the limit of their errors. $R_{N(L)}$ bond distances in the GS DFT-PBE0 optimized structure are reported for comparison, separately averaged for each type of ligand L.

Results of GS EXAFS fit and test fit on PHP using GS model			
Parameters	GS DFT average bond lengths	GS EXAFS fit	PHP tentative EXAFS fit
Indipendent points		21	21
Number of variables		6	6
R-factor		0.011	0.010
S_0^2		0.95 ± 0.06	0.94 ± 0.06
ΔE (eV)		0.8 ± 0.5	-0.4 ± 0.6
$R_{N(py)}$ (Å)	2.14	2.09 ± 0.03	2.12 ± 0.03
$\sigma^2_{N(py)}$ (Å^2)		0.0032 ± 0.0008	0.0041 ± 0.0009
N_{py}^{fit} (N_{py}^{eff})		2 (2)	2 (1)
$R_{N(bpy)}$ (Å)	2.08	2.05 ± 0.02	2.04 ± 0.01
$\sigma^2_{N(bpy)}$ (Å^2)		0.0026 ± 0.0008	0.0023 ± 0.0008
N_{bpy}^{fit} (N_{bpy}^{eff})		4 (4)	4 (4)

C5. Details on PHP differential EXAFS analysis

The PHP structure has been primarily modeled simply removing from the set of SS and MS paths generated for the GS structure all the paths related to one of the two py rings, except for that involving

the first shell N atom, maintained to simulate the almost isoelectronic O atom of the water molecule coordinated to the metal centre. The fitting model is identical to that described in Section C4 for the GS spectrum, apart from the use of two additional parameters to account for the newly coordinated solvent molecule, i.e. the bond distance $R_{Ru–O(H2O)}$ and the oxygen DW σ^2_O.

Fixing the amplitude S_0^2 at the GS value, the array of parameters P is then composed in the following way: P = {ΔE, ΔR_{bpy}, ΔR_{py}, ΔR_O, σ^2_{bpy}, σ^2_{py}, σ^2_O}, where the parameters ΔR_L indicates the bond length variations from the DFT-optimized structure for ligands L = bpy, py and H_2O respectively. Our application of the differential method is based on the computation of a series of variational grids for a sub-set of parameters P', with the remaining parameters fixed to the GS best fit values: P_{GS} = {ΔE = 0.8 eV, ΔR_{bpy} = – 0.03 Å, ΔR_{py} = –0.05 Å, $\Delta R_O = \Delta R_{py}$ = 0.05 Å, σ^2_{bpy} = 0.0026 Å^2, σ^2_{py} = 0.0032 Å^2, $\sigma^2_O = \sigma^2_{py}$}. Operationally, we selected a subspace P' of dimension N', planning a series of reasonable values for the variation of each parameter (centered on the GS value for that parameter). Hence, we computed a N'-dimensional grid where the i^{th} node is a simulated $\chi_i^{PHP}(q)$ curve, characterized by the parameters P_i= = {P'_i; P_{GS}} and obtained by summing the scattering paths for the PHP structure calculated via the FEFF code, setting the parameters to selected values.

The minimization of the R-factor between the experimental differential curve $\Delta\chi^{PHP}_{exp}(q) = \chi^{PHP}_{exp}(q) - \chi^{GS}_{exp}(q)$ and each of the simulated differential spectra $\Delta\chi_i^{PHP}(q) = \chi_i^{PHP}(q) - \chi^{GS}_{fit}(q)$ is performed using a dedicated script. The minimization results can be represented in terms of R-factor(p_1, … , p_N) surfaces, where N is the number of parameters effectively varied.

The simultaneous exploration of the whole 7-dimensional parameter space with reasonable ranges for the variation of the parameters is not feasible, due to the extremely high human and machine time demand that such operation would require. However, supported by DFT calculations and general considerations about the "natural" correlations expected among the parameters, it is possible to properly select an informative sequence of subspaces P' to be scanned. We explored a consecutive series of four 2D or 3D sub-spaces, with (a) P' = {P_{GS}; ΔE; ΔR_{bpy}}; (b) P' = {P_{GS}; ΔR_O, σ^2_O}; (c) P' = {P_{GS}; σ^2_O = 0.0055 Å^2, ΔE, ΔR_{bpy}, ΔR_O}; (d) P' = {P_{GS}; ΔR_{py}, ΔR_O}, trying to approach the global minimum in the whole 7D space.

After the partial minimization cycles (a) – (d), an extended exploration of the 4D space including the energy shift and the three distortions along the bonds Ru−N(bpy), Ru−N(py) and Ru−O(H_2O), i.e. P' = {P_{GS}; σ^2_O = 0.0055 Å^2, ΔE, ΔR_{bpy}, ΔR_{py}, ΔR_O}, was performed. DW values where fixed to GS values for bpy and py units, while the DW accounting for vibrations along the Ru−O(H_2O) bond was set to the value σ^2_O = 0.0055 Å^2, obtained from the minimization cycle (b). Among the 258 $\Delta\chi^{PHP}_i(q)$ simulated and tested curves, the lower R-factor value of 0.147 is obtained in correspondence of the array {P_{GS}; σ^2_O = 0.0055 Å^2, ΔE = –1.0 eV, ΔR_{bpy} = –0.03 Å, ΔR_{py} = –0.07 Å, ΔR_O = –0.02 Å}. The $\Delta\chi^{PHP}_i(q)$ calculated in correspondence of these values is then selected as best differential fit for the experimental $\Delta\chi^{PHP}_{exp}(q)$ and will be hereinafter mentioned as $\Delta\chi^{PHP}_{fit}(q)$.

Table C2 compares (i) $R_{Ru–N(L)}$ bond distances (where L = bpy, py or H_2O) from DFT geometry optimization of GS and PHP, separately averaged for each type of ligand, see also Section A; (ii) GS standard EXAFS fitting results; (iii) parameters' values obtained using the differential method for the PHP structural refinement.

Table C2. Results from standard EXAFS analysis of GS and from differential analysis of PHP spectrum (parameters P' selected for variation are highlighted in red). DFT-PBE0 first shell $R_{Ru-N(L)}$ bond distances (where L= bpy, py, H_2O) for GS and PHP, separately averaged for each type of ligand L, are reported for comparison. The error on PHP refined parameters corresponds to the step separating two contiguous nodes on the minimization grid employed.

Optimized Parameters for GS and PHP				
Parameters	DFT optimization		EXAFS fit	
	GS average bond lengths	PHP average bond lengths	GS (Standard analysis)	PHP (Differential analysis)
Indipendent points			21	-
Number of variables			6	5 refined variables
R-factor			0.011	0.147*
S_0^2			0.95 ± 0.06	0.95 ± 0.06
ΔE (eV)			0.8 ± 0.5	-1.0±0.5
R_{bpy} (R_{bpy}) (Å)	2.08	2.07	2.05 ± 0.02	2.05 ±0.01
σ^2_{bpy} (Å^2)			0.0026 ± 0.0008	0.0023 ± 0.0008
R_{py} (R_{py}) (Å)	2.14	2.13	2.09 ± 0.03	2.07 ± 0.01
σ^2_{py} (Å^2)			0.0032 ± 0.0008	0.0041 ± 0.0009
R_O (R_O) (Å)	-	2.21	-	2.12 ±0.01
σ^2_O (Å^2)			-	0.005 ±0.001

*R-factor defined according to eq. (S1), not directly comparable with the fit goodness figure reported for GS standard EXAFS fit.

Differential refinement indicates an almost unvaried bond length for the bpy rings with respect to the GS value, while the bond length for the remaining py ring appears to be contracted from 2.09 Å to 2.07 Å. For the newly coordinated water molecule, a noticeable increase on Ru−O(H_2O) bond length of 0.03 Å with respect to the average Ru−N(py) GS bond distance is obtained. Such feature is associated with an increase of the corresponding DW, from σ^2_{py} = (0.0032 ± 0.0008) Å^2 to σ^2_O = (0.005 ± 0.001) Å^2, in good agreement with the substitution of a py ring with a smaller and more vibrationally-active water ligand.

DFT-optimized geometries are key starting points for the analysis, especially when working close to the state-of-art sensitivity limit of the XAS technique and when the complexity of the case of study unavoidably requires some approximations (e.g. choosing a meaningful variation range for a structural parameter, or defining a priority scale for testing different kinds of distortions). Moreover, the theoretical results can also be used as a final test for the reliability of the experimental data interpretation, in a synergic cross-comparison useful to make us aware of specific limits and advantages for each approach.

In the studied case, a systematic slight underestimation of the EXAFS-refined bond lengths is found respect to the values from DFT geometry optimization, as already obtained for this complex and other analogues.[25, 26] Hence, a more meaningful comparison can be done focusing on relative variations moving from GS to PHP structure, rather than on the absolute values. The more striking result is the good DFT/ EXAFS agreement in pointing out the elongation of the PHP Ru−O(H_2O) bond respect to previous GS py. Regarding the bond distortions of the py and bpy ligands, DFT average values indicates a slight contraction for both ligand types, while, as mentioned before, the differential EXAFS refinement points out an almost unvaried bond length for the bpy rings with respect to the GS value,

and a more evident –0.02 Å contraction along the Ru−N(py) bond. Checking the DFT Ru bond lengths separately for each first-shell neighbor (see Table A2), it is possible to realize how the bond distances for all the rings belonging to the two bpy units are almost unchanged, except the one of the ring in *trans* position to the water-substituted py (containing the N atom labeled as N1, see Scheme A1). Imaging to separate a bpy unit in two independent py rings, the major changes foreseen by DFT can be summarized in an elongation of the Ru−O(H_2O) bond and in a contraction of the Ru−N1 bond involving the ligand in *trans* position.

However, the model adopted for EXAFS data interpretation optimizes the distortions for the two N(bpy) atoms with a single ΔR_{bpy} parameter, and does not account for independent distortions along each of the Ru−N(bpy) bond axis. A major limit of this approach, adopted to limit the number of parameters, relies in the difficult in discriminating between single py rings and pairs of rings grouped in bpy units "artificially" tied in an identical motion. Therefore, the pronounced contraction ΔR_{py} is likely to be associated to the bond contraction for the single ring in *trans* to O (H_2O) of a bpy unit, and it has not been correctly assigned due to the vinculum on ΔR_{bpy}. This hypothesis is also supported by the strong anti-correlation found between ΔR_{py} and ΔR_O.

Finally, in Figure C4a are reported the six possible 2D cuts of the 4D R-factor surface as a function of the parameter array (ΔE, ΔR_{bpy}, ΔR_{py}, ΔR_O), obtained by fixing to the values found in correspondence of the minimum a couple of parameters each time. The high quality of the fit can be appreciated in Figure C4b, where the experimental differential spectrum $\Delta\chi^{PHP}{}_{exp}(q)$ (black circles) is compared with the $\Delta\chi^{PHP}{}_{fit}(q)$ best fit curve (magenta solid line). Finally, in Figure C4c, a comparison between the not-differential GS and PHP experimental spectra with their respective best fit curves $\chi^{GS}{}_{fit}(q)$ and $\chi^{PHP}{}_{fit}(q)$ is reported.

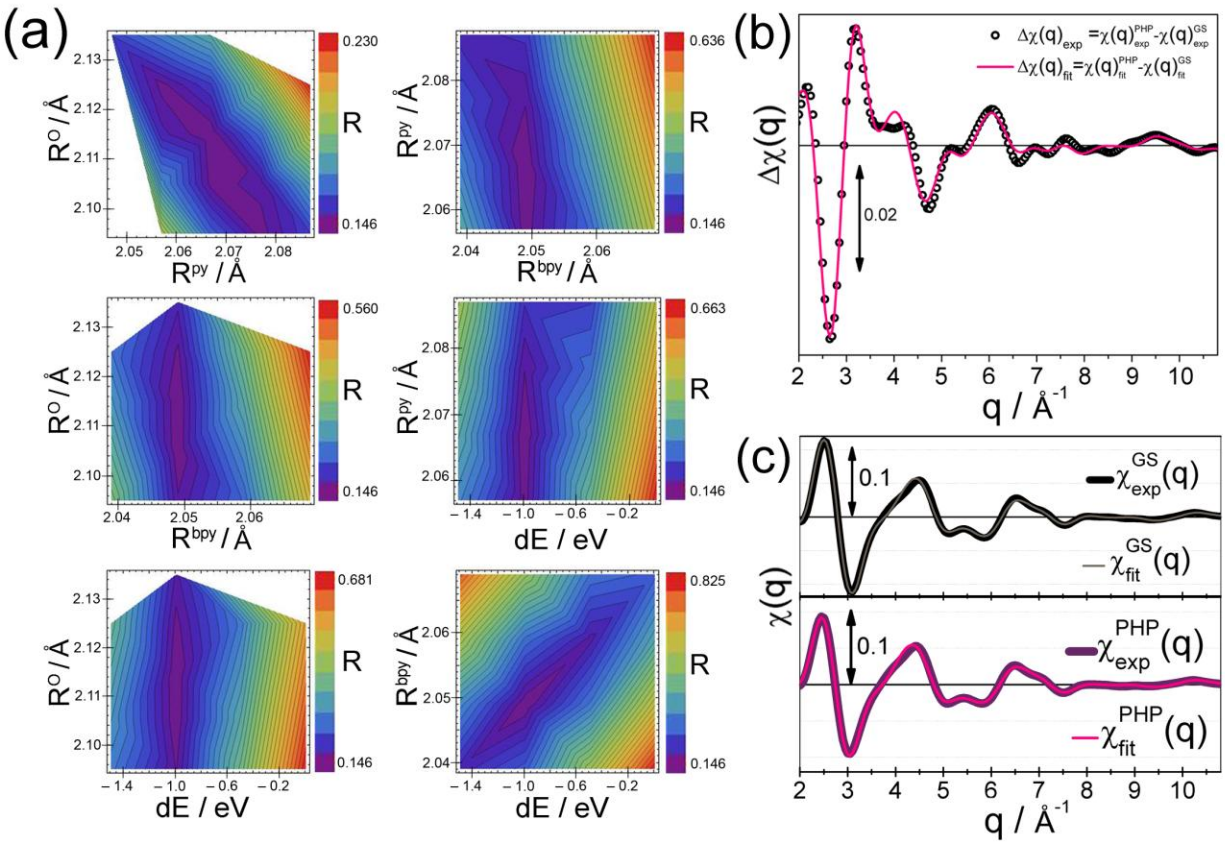

Figure C4. Results from the final minimization procedure of the PHP differential EXAFS analysis, in the 4D space P' = {P_{GS}; σ^2_O = 0.0055 Å^2, ΔE, ΔRb_{bpy}, ΔR_{py}, ΔR_O}. (a) 2D cuts of the 4D R-factor (ΔE, ΔRb_{bpy}, ΔR_{py}, ΔR_O) surface, obtained by fixing couples of parameters each time to the values found in correspondence of the minimum. (b) Comparison between experimental differential spectrum $\Delta\chi^{PHP}{}_{exp}(q)$ (black circles) and $\Delta\chi^{PHP}{}_{fit}(q)$ best-fit curve (pink solid line). (c) Comparison between the not-differential GS (upper part) and photoproduct (bottom part) experimental spectra with correspondent best fit curves $\chi^{GS}{}_{fit}(q)$ and $\chi^{GS}{}_{fit}(q)$, obtained from standard EXAFS fit and differential EXAFS refinement respectively.

C6. Details on XTA fitting procedure

C6.1. Excited state dynamics

A widely accepted general scheme for the excited-state dynamics of ruthenium polypyridyl complexes is the following:

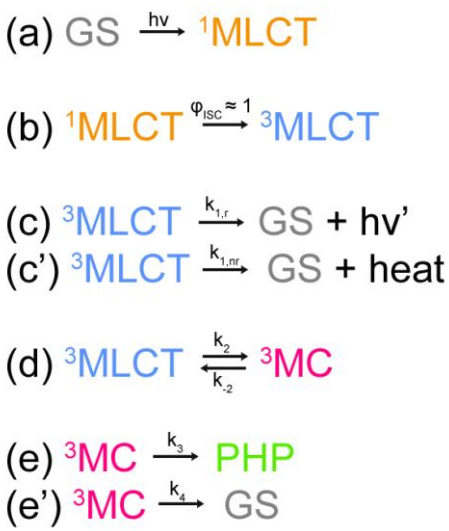

Scheme C3

In the specific case of aqueous *cis*-$[Ru(bpy)_2(py)_2]Cl_2$, $k_{1,r}$ and $k_{1,nr}$ (eq. c and c' in Scheme C3) can be considered as negligible. Moreover $k_{-2} << k_2$, resulting in irreversible population of the ^{3}MC state from the ^{3}MLCT.[27-30] According to such a scenario and considering the OTA time components together with a 20% photochemical yield φ, the populations of the ^{3}MLCT ES and PHP species, that mainly contribute to XTA signal at the investigated time-points, can be calculated using the set of equations (S2) and represented as in Figure C5:

$$N_{^3MLCT} = \exp\left(-\frac{t}{\tau_{long}}\right)$$
$$N_{PHP} = \phi[1 - N_{^3MLCT} - \Delta(\tau_{short})] \qquad \text{(S2)}$$

The $\Delta(\tau_{short})$ parameter is related to the shorter OTA time component, and is given by eq. (S3):

$$\Delta(\tau_{short}) = \exp\left(-\frac{t}{\tau_{short}}\right)(1 - N_{^3MLCT}) \qquad \text{(S3)}$$

$\Delta(\tau_{short})$ is a minor correction, that slightly delays the PHP formation along the relaxation cascade from ^{3}MLCT ES. Its effect can be appreciated only at the earlier time-delay investigated (150 ps) and it is negligible for the following delays τ = 500 ps and 3000 ps, that actually provide the more reliable structural information. Such effect can be tentatively related to the ^{3}MC/photochemistry pathway, and eventually to complex solvent-mediated interactions. However, further investigation is needed to confirm this assignment.

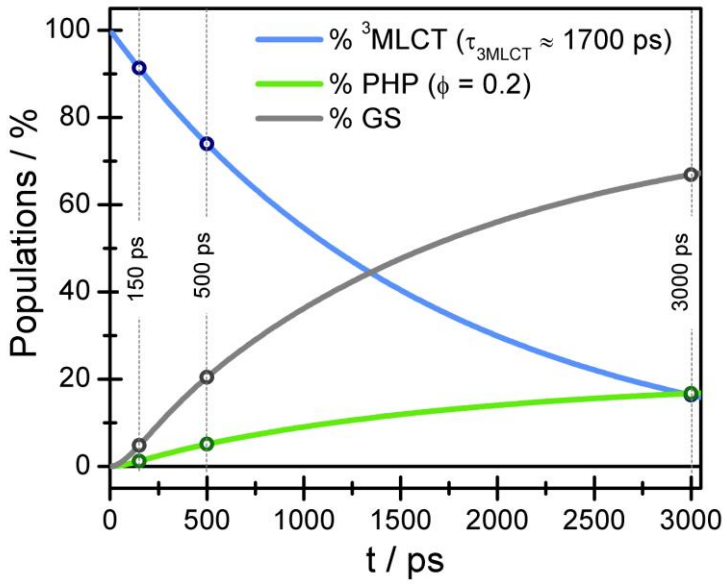

Figure C5. Time evolution of ^{3}MLCT population (blue solide line) and PHP percentage (green solid line) calculated according to Scheme C3 and eqs (S2). Circles and vertical dashed lines are placed in correspondence of the XTA experimental time delays.

Such information was employed to orientate the XTA differential fitting procedure. Briefly, the optimized amplitudes f^{PHP} and f^{3MLCT} relative to the PHP and ^{3}MLCT components of the XTA signal were searched within an interval defined by the estimated populations. In particular, the ratio f^{PHP}/f^{3MLCT} was constrained to vary around the population ratio $R^{3MLCT/PHP}$ calculated using eqs. (S2) and assuming a tolerance of $\pm$ 0.2 $R^{3MLCT/PHP}$ with respect to the center of the range (vide infra, in particular Section C6.5). In this way a considerable stabilization in the fit outcomes was achieved.
The population of ^{3}MLCT and the PHP percentage estimated for the three time-delays investigate by XTA (150 ps, 500 ps and 3000 ps), according to eqs (2), are reported in Table C3.

Table C3. Population of ^{3}MLCT and PHP percentage for τ = 150 ps, 500 ps and 3000 ps, estimated using eqs. (S2), according to the assignment $\tau_{3MLCT} = \tau_{long}$ = 1700 ps for the longer OTA component. The ratio R = % ES(τ_{long}) / % PHP is used to orient the XTA fitting procedure (see also Section C6.5).

Time-delay (ps)	% ^{3}MLCT (τ_{long})	% PHP	$R^{ES/PHP}$ = % ES(τ_{long}) / % PHP [($R^{ES/PHP}$ – 0.2 $R^{ES/PHP}$): ($R^{ES/PHP}$ + 0.2 $R^{ES/PHP}$)]
150	91.3	1.2	76 [61:91]
500	73.9	5.1	15 [13:18]
3000	16.3	16.7	1.0 [0.8:1.2]

C6.2. Detailed description of XTA fitting results

As mentioned before, we developed a fitting strategy based on the combination of the two dominant structural components , i.e. the PHP and the long-lived ^{3}MLCT ES. The possibility of a slightly

different energy shift due to the use of different beamlines to acquire the static PHP spectrum and the XTA dataset was considered by repeating the fit in correspondence of different ΔE values for the PHP simulated $\chi^{PHP}_{fit}(q)$ curve.

The fitting procedure, implemented using a dedicated script, can be summarized in the steps listed below.

For a selected time delay τ and a selected value of PHP energy shift ΔE_i^{PHP}:

(i) The experimental $\Delta\chi(q, \tau)$ curve, as well as the simulated $\chi^{PHP}_{fit}(\Delta E_i^{PHP}, q)$ and $\chi^{GS}_{fit}(q)$ curves are imported, and the theoretical PHP component $\Delta\chi^{PHP}(\Delta E_i^{PHP}, q) = \chi^{PHP}_{fit}(\Delta E_i^{PHP}, q) - \chi^{GS}_{fit}(q)$ is calculated.

(ii) An array of $\chi^{ES}_i(P_{GS}; P', q)$ simulated curves (ES = ^{3}MLCT), obtained from systematic distortions of the GS structure the in the parameter subspace P' is imported.

(iii) the experimental $\Delta\chi(q, \tau)$ curve is fitted with a linear combination of PHP and long-lived ES contributions for each $\chi^{ES}_i(P_{GS}; P', q)$ curve, i.e. $\Delta\chi(q, \tau) = f_i^{PHP}\Delta\chi^{PHP}(\Delta E_i^{PHP}, q) + f_i^{ES}\Delta\chi^{ES}_i(P_{GS}; P', q)$, where $\Delta\chi^{ES}_i(P_{GS}; P', q) = \chi^{ES}_i(P_{GS}; P', q) - \chi^{GS}_{fit}(q)$ and the amplitudes f_i^{PHP} and f_i^{ES} are the optimized variables; a R_i R-factor is calculated for each simulated ES structure.

The minimum R_i value is used to select the best fit for the experimental $\Delta\chi(q, \tau)$ curve and to determine the optimized values of P' parameters and amplitudes f^{PHP} and f^{ES}. A complete overview on the fitting results is reported in Table C4.

Table C4. Detailed report on results from the 30-fits differential refinement procedure of XTA data. For all investigated time delays, the optimized values obtained for bond lengths $R_{Ru–N1}$, $R_{Ru–N53}$, for PHP and ES energy shifts (ΔE^{PHP} and ΔE^{ES}, respectively) and for amplitudes f^{PHP} and f^{PHP} related to PHP and ES component (as well as the value of the ratio $R^{ES/PHP}$) are listed.

Optimized parameters values from differential fitting procedure of XTA data				
$\tau_{3MLCT} = \tau_{long}$				
τ (ps)	$R_{Ru–N1}$ (Å)	$R_{Ru–N53}$ (Å)	ΔE^{PHP} ΔE^{ES} (eV)	f^{PHP} f^{ES} ($R^{ES/PHP}$)	R-factor
150	2.07	2.06	-1.99 -1.49	0.002 0.134 (67.0)	0.284
500	2.03	2.20	0.49 -0.99	0.020 0.271 (13.5)	0.180
3000	2.03	2.16	-0.99 -0.99	0.084 0.100 (1.2)	0.378

C6.3. Repetition of the fitting-procedure assuming $\tau_{long} = \tau_{3MC}$

As a final test, we explored the effect of a reversal assignment of OTA time-component, i.e. τ_{3MC}= τ_{long}=1700 ps, on the XTA fitting results. For the sake of clarity, hereinafter we will indicate as model

(1) the previously discussed assignment, $\tau_{3MLCT} = \tau_{long} = 1700$ ps, and as model (2) the one corresponding to the reversal assignment $\tau_{3MC} = \tau_{long} = 1700$ ps.

A comparison between the fitting results obtained using model (1) or (2) is depicted in Figure C5. Here, the R-factor values found for corresponding fits are plotted as a function of the only parameter associated to the PHP component i.e. its energy shift ΔE_i^{PHP}. Every point in the plots is thus associated with a minimum in the sub-space P' = {P_{GS}; ΔE^{ES}, R_{Ru-N1}, R_{Ru-N53}}, separately explored for ^{3}MLCT (model (1), blue points in Figure C5) and ^{3}MC (model (2), purple points in Figure C5) geometries. For more details on the selection of the structural parameters to refine and their variation grids, see the following Section C6.4.

Maintaining the ΔE_i^{PHP} value inside a reasonable range for variation, the two series of fits are very well-separated for all the three time delays analyzed, and the fit goodness is systematically higher (lower R-factor values) in the case of model (1). This evidence allows to definitely assign the longer OTA time component $\tau_{long} = 1700$ ps to the ^{3}MLCT ES.

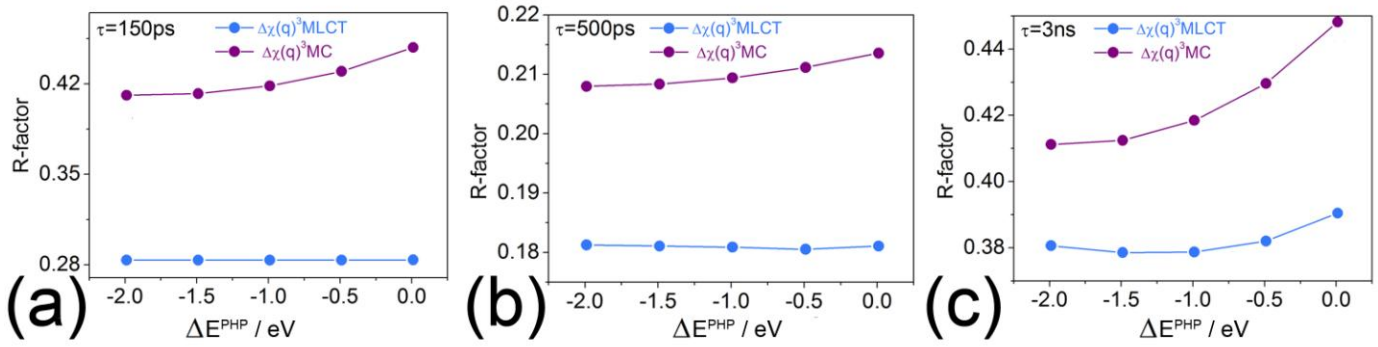

Figure C5. Results from the complete XTA fitting procedure, separately reported for each time delay (150, 500 and 3000 ps in part (a), (b) and (c), respectively). The R-factor value for each fit is plotted as a function of the only parameter associated to the PHP component, i.e. its energy shift ΔE_i^{PHP}.

C6.4. Minimization grids selected to model and optimize ^{3}MLCT and ^{3}MC structures

The approach adopted for differential refinement of the time-resolved dataset was that already discussed in details for PHP differential analysis (see Section C5). In the case of XTA analysis, the DFT role in directing the selection of what bond lengths preferentially modify is fundamental. However, the differential approach guarantees an independent experimental validation for the theoretical geometries. In Table C5 Ru first-shell bond distances from DFT geometry optimization of ^{3}MLCT and ^{3}MC ES structures are summarized (see also Section A). Analyzing the values reported in Table C5, it can be noticed that the main variations occur in correspondence of Ru−N1(bpy) and Ru−N53(py) bonds, for both the considered ES structures. Also the Ru−N2 bond is perturbed but, to limit the number of parameters, the selection of bonds to be systematically modified was restricted to Ru−N1(bpy) and Ru−N53(py) only. Starting from the EXAFS paths generated for the GS structure, we isolated the SS and MS paths involving the 6+6 atoms of the two rings selected, carefully adjusting the paths degeneracy, and varied independently the two bond distances R_{Ru-N1} and R_{Ru-N53}.

Table C5. Ru first-shell bond distances from DFT geometry optimization of ^{3}MLCT and ^{3}MC structures, distinguishing all the 6 bonds in which the Ru-center is involved. Bonds distances selected for variational minimization are highlighted in red.

^{3}MLCT structural parameters from DFT geometry optimization					
Ru−N1(bpy)	Ru−N2(bpy)	Ru−N13(bpy)	Ru−N14(bpy)	Ru−N42(py)	Ru−N53(py)
2.03	2.06	2.07	2.11	2.14	2.17
^{3}MC structural parameters from DFT geometry optimization					
Ru−N1(bpy)	Ru−N2(bpy)	Ru−N13(bpy)	Ru−N14(bpy)	Ru−N42(py)	Ru−N53(py)
2.37	2.16	2.10	2.09	2.14	2.80

The explored sub-space P' is constituted for both the possible ESs by P' = {P_{GS}; ΔE^{ES}, $R_{Ru–N1}$, $R_{Ru–N53}$}; the {$R_{Ru–N1}$, $R_{Ru–N53}$} variation grids for the ^{3}MLCT and ^{3}MC ESs are composed in the following way: (i) ^{3}MLCT variation grid (employed for the principal model (1)) comprises $R_{Ru–N1}$ values from 2.00 Å to 2.22 Å in steps of 0.02 and $R_{Ru–N53}$ values from 1.96 Å to 2.24 Å in steps of 0.02; (ii) ^{3}MC variation grid (employed for the final check using model (2)) includes $R_{Ru–N1}$ values from 2.15 Å to 2.45 Å in steps of 0.05 Å and $R_{Ru–N53}$ values from 2.55 Å to 3.15 Å in steps of 0.1 Å. The bond length distortions subspace is complemented with a wide-range ΔE^{ES} scan, from – 2.0 eV to 2.0 eV, meshed in 0.5 eV steps. The fitting procedure was repeated for each time delay, using a set of 5 values for ΔE_i^{PHP}, comprised in the – 2.0 – 0.0 eV and regularly spaced of 0.5 eV.

C6.5. Constrains for the optimization of f^{PHP} and f^{ES} amplitudes

An important point to be discussed involves the definition of some constrains for the optimization of f^{PHP} and f^{ES} amplitudes, to stabilize the fitting procedure and to orient the results towards chemically meaningful values, according to estimated populations. Indeed, the main features of simulated $\Delta\chi^{ES}$ curves (maxima and minima positions and overall curve shape) are quite similar for all the states/species here considered, i.e. ES = ^{3}MLCT in the principal model (1), ^{3}MC in the control model (2), and PHP (at least considering the portions of the variation grids near to DFT theoretical values). The striking difference relies in the amplitude of the $\Delta\chi^{ES}$ curves, especially comparing the simulated spectra $\Delta\chi^{3MLCT}$ and $\Delta\chi^{PHP}$ with $\Delta\chi^{3MC}$, where the highly pronounced structural distortions cause a huge increase in the differential amplitude. This can explain why a completely not-constrained two components fits for the amplitude optimization was found to be very unstable, due to the high correlation between f^{PHP} and f^{ES} amplitudes guessed in the fit. We decided to employ the percentages calculated using eqs (2) to orient the fit procedure. The ratio $R^{ES/PHP}$ = %ES (τ_{long}) / %PHP accounted for the relative amplitude expected between the two components included in the fit, and was used to define the fit constrains, overcoming the problem on the unknown excitation yield (acting as a global scale factor for the experimental $\Delta\chi(q, \tau)$ curve). The amplitudes f^{PHP} and f^{ES} were constrained to vary around the calculated value of $R^{ES/PHP}$, assuming a tolerance of ± 0.2 $R^{ES/PHP}$ with respect to the centre of the range. We obtained in this way a considerable stabilization in the fit outcomes.

C6.4. Graphical representation of XTA fit results for τ = 150 ps

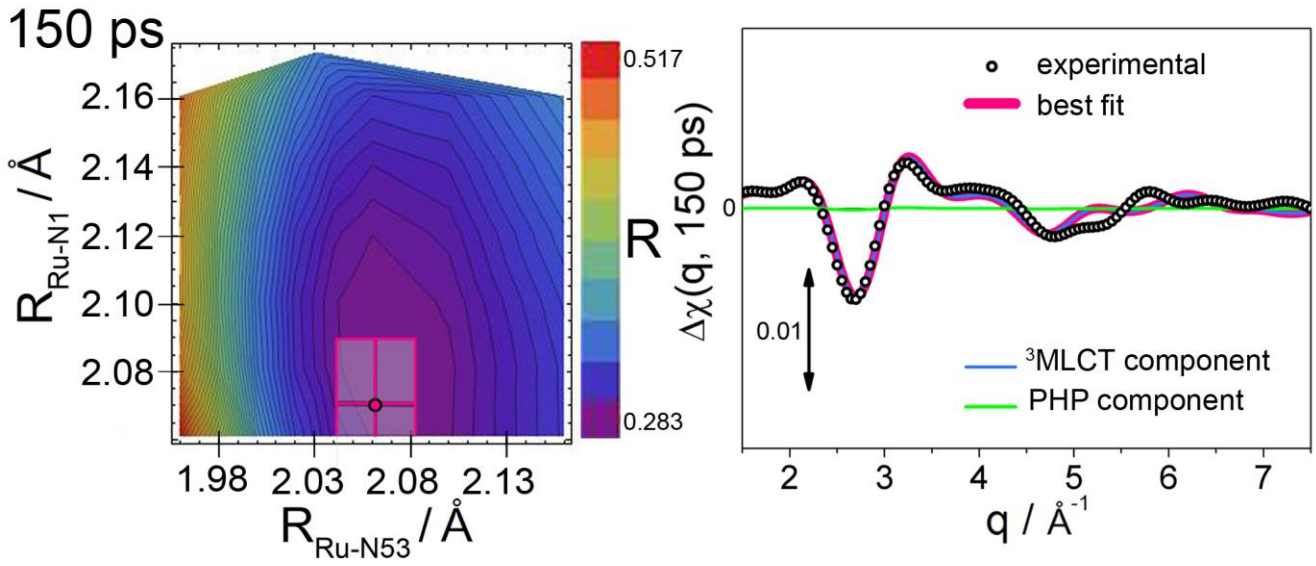

Figure C6. Surface contour plots of the fit R-factor as a function of $R_{Ru–N1}$ and $R_{Ru–N53}$ and best fit $\Delta\chi_{fit}(q,\tau)$ curves corresponding to the R-factor surface global minimum (magenta solid lines), superimposed to experimental XTA data (black circles) for τ = 150 ps. The magenta box identifies the experimental error interval (± 0.02 Å on both $R_{Ru–N1}$ and $R_{Ru–N53}$ axis) around the minimum localized at the lines' crossing point. The fit components relative to the ^{3}MLCT and PHP contributions to the overall XTA signal are indicated as blue and green solid lines respectively.

References

1. M. J. Frisch, G. W. Trucks, H. B. Schlegel, G. E. Scuseria, M. A. Robb, J. R. Cheeseman, G. Scalmani, V. Barone, B. Mennucci, G. A. Petersson, H. Nakatsuji, M. Caricato, X. Li, H. P. Hratchian, A. F. Izmaylov, J. Bloino, G. Zheng, J. L. Sonnenberg, M. Hada, M. Ehara, K. Toyota, R. Fukuda, J. Hasegawa, M. Ishida, T. Nakajima, Y. Honda, O. Kitao, H. Nakai, T. Vreven, J. Montgomery, J. A., J. E. Peralta, F. Ogliaro, M. Bearpark, J. J. Heyd, E. Brothers, K. N. Kudin, V. N. Staroverov, R. Kobayashi, J. Normand, K. Raghavachari, A. Rendell, J. C. Burant, S. S. Iyengar, J. Tomasi, M. Cossi, N. Rega, N. J. Millam, M. Klene, J. E. Knox, J. B. Cross, V. Bakken, C. Adamo, J. Jaramillo, R. Gomperts, R. E. Stratmann, O. Yazyev, A. J. Austin, R. Cammi, C. Pomelli, J. W. Ochterski, R. L. Martin, K. Morokuma, V. G. Zakrzewski, G. A. Voth, P. Salvador, J. J. Dannenberg, S. Dapprich, A. D. Daniels, Ö. Farkas, J. B. Foresman, J. V. Ortiz, J. Cioslowski and D. J. Fox, Gaussian, Inc., Wallingford, CT, Revision A.1 edn., 2009.
2. A. D. Becke, *J. Chem. Phys.*, 1993, **98**, 5648-5652.
3. C. T. Lee, W. T. Yang and R. G. Parr, *Phys. Rev. B*, 1988, **37**, 785-789.
4. C. Adamo and V. Barone, *J. Chem. Phys.*, 1999, **110**, 6158-6170.
5. C. Adamo, G. E. Scuseria and V. Barone, *J. Chem. Phys.*, 1999, **111**, 2889-2899.
6. P. J. Hay and W. R. Wadt, *J. Chem. Phys.*, 1985, **82**, 270-283.
7. A. D. McLean and G. S. Chandler, *J. Chem. Phys.*, 1980, **72**, 5639-5648.
8. A. Vlcek and S. Zalis, *Coord. Chem. Rev.*, 2007, **251**, 258-287.
9. V. Barone and M. Cossi, *J. Phys. Chem. A*, 1998, **102**, 1995-2001.

10. M. Cossi and V. Barone, *J. Chem. Phys.*, 2001, **115**, 4708-4717.
11. M. Cossi, N. Rega, G. Scalmani and V. Barone, *J. Comput. Chem.*, 2003, **24**, 669-681.
12. J. M. Tao, J. P. Perdew, V. N. Staroverov and G. E. Scuseria, *Phys. Rev. Lett.*, 2003, **91**.
13. Y. Zhao and D. G. Truhlar, *Theor. Chem. Acc.*, 2008, **120**, 215-241.
14. C. Adamo and V. Barone, *J. Chem. Phys.*, 1998, **108**, 664-675.
15. J. Heyd and G. E. Scuseria, *J. Chem. Phys.*, 2004, **121**, 1187-1192.
16. M. E. Casida, C. Jamorski, K. C. Casida and D. R. Salahub, *J. Chem. Phys.*, 1998, **108**, 4439-4449.
17. R. E. Stratmann, G. E. Scuseria and M. J. Frisch, *J. Chem. Phys.*, 1998, **109**, 8218-8224.
18. N. M. O'Boyle, A. L. Tenderholt and K. M. Langner, *J. Comput. Chem.*, 2008, **29**, 839-845.
19. E. F. Pettersen, T. D. Goddard, C. C. Huang, G. S. Couch, D. M. Greenblatt, E. C. Meng and T. E. Ferrin, *J. Comput. Chem.*, 2004, **25**, 1605-1612.
20. B. Ravel and M. Newville, *J. Synchrot. Radiat.*, 2005, **12**, 537-541.
21. C. Bressler, C. Milne, V. T. Pham, A. El Nahhas, R. M. van der Veen, W. Gawelda, S. Johnson, P. Beaud, D. Grolimund, M. Kaiser, C. N. Borca, G. Ingold, R. Abela and M. Chergui, *Science*, 2009, **323**, 489-492.
22. S. Nikitenko, A. M. Beale, A. M. J. van der Eerden, S. D. M. Jacques, O. Leynaud, M. G. O'Brien, D. Detollenaere, R. Kaptein, B. M. Weckhuysen and B. W., *J. Synchrot. Radiat.*, 2008, **15**, 632–640.
23. L. Salassa, E. Borfecchia, T. Ruiu, C. Garino, D. Gianolio, R. Gobetto, P. J. Sadler, M. Cammarata, M. Wulff and C. Lamberti, *Inorg. Chem.*, 2010, **49**, 11240-11248.
24. L. Salassa, C. Garino, G. Salassa, C. Nervi, R. Gobetto, C. Lamberti, D. Gianolio, R. Bizzarri and P. J. Sadler, *Inorg. Chem.*, 2009, **48**, 1469-1481.
25. L. Salassa, D. Gianolio, C. Garino, G. Salassa, E. Borfecchia, T. Ruiu, C. Nervi, R. Gobetto, R. Bizzarri, P. J. Sadler and C. Lamberti, *J. Phys.: Conf. Ser.*, 2009, **190**, 012141.
26. L. Salassa, T. Ruiu, C. Garino, A. M. Pizarro, F. Bardelli, D. Gianolio, A. Westendorf, P. J. Bednarski, C. Lamberti, R. Gobetto and P. J. Sadler, *Organometallics*, 2010, **29**, 6703-6710.
27. J. V. Caspar and T. J. Meyer, *Inorg. Chem.*, 1983, **22**, 2444-2453.
28. W. M. Wacholtz, R. A. Auerbach, R. H. Schmehl, M. Ollino and W. R. Cherry, *Inorg. Chem.*, 1985, **24**, 1758-1760.
29. M. Adelt, M. Devenney, T. J. Meyer, D. W. Thompson and J. A. Treadway, *Inorg. Chem.*, 1998, **37**, 2616-2617.
30. D. W. Thompson, C. N. Fleming, B. D. Myron and T. J. Meyer, *J. Phys. Chem. B*, 2007, **111**, 6930-6941.